Adam P. Hitchcock

# 5 PEMFC analysis using soft X-ray spectromicroscopy: methods and applications

## 5.1 Introduction

Polymer electrolyte membrane fuel cells (PEMFC) [1–3] offer many advantages over competing electric power systems for mobile applications. However, cost, durability and refueling issues need to be solved before widespread adoption will occur. In order to improve performance and reduce cost, a detailed understanding of the limiting factors is needed. In many cases quantitative, high spatial resolution, species-specific 2D and 3D imaging is required in order to understand the links between chemistry, structure/morphology and performance and thereby enable improvements through rational design. While analytical electron microscopes are superb at imaging and detailed analysis of radiation resistant components such as atomic-level studies of core-shell catalyst particles [4, 5], their capabilities are limited when applied to the very radiation sensitive perfluorosulfonic acid (PFSA)-ionomer, which is essential for proton conductivity in the electrodes. Reliable and comprehensive 2D and 3D structures at many different length scales are needed to improve modeling of PEMFC operation under normal and stressed conditions [6]. Areas where soft X-ray scanning X-ray microscopy (SXM) have played a role in achieving a better understanding include: (i) optimal use of Pt by optimization of the ionomer distribution in PEMFC electrodes; (ii) understanding degradation phenomena, which limit lifetime and efficiency; (iii) investigation of novel catalytic systems such as the 3M nanostructured thin film (NSTF) species and electroless deposition of Pt

**Adam P. Hitchcock,** Dept. of Chemistry & Chemical Biology, Brockhouse Institute for Materials Research, McMaster University, Hamilton, ON, L8S 4M1, Canada

on membranes. This chapter describes SXM and its applications to these types of PEMFC studies.

My group has collaborated with industrial partners (Ballard Power Systems; the Automotive Fuel Cell Co-operation Corporation, AFCC; and 3M) and the Canadian Catalyst Research for Polymer Electrolyte Fuel Cells (CaRPE-FC) network over the past 12 years to develop SXM methods and apply them to PEMFC materials, systems and devices. Early work focused on developing and validating a method to use scanning transmission X-ray microscopy (STXM) [7–9] for quantitative 2D projection mapping of PFSA in PEMFC cathodes [10–12]. Ionomer mapping by STXM became a standardized analytical method for AFCC who used it extensively from 2013 to 2016 to help guide their research into cathode optimization. In parallel to that activity, and in collaboration with industry partners, we studied: Pt migration into the membrane (PTIM) [13, 14]; effect of the type of carbon support on carbon corrosion [15]; the fate of the polymer support in NSTF catalysts through their fabrication and implementation in an membrane electrode assembly (MEA) [16, 17]; and the Pt-membrane interface in electroless deposited Pt on membranes [18, 19]. In recent years, my group has concentrated on further improvements in SXM methodology as applied to PEMFC, including: evolving PFSA-in-cathode mapping from 2D to 3D through use of angle-scan tomography [20–23]; porosity mapping [24]; better understanding of radiation damage of PFSA by electron beams [25, 26], ion beams [27] and X-rays [28, 29]; improving spatial resolution through the emerging SXM method of ptychography [30, 31]; development of a STXM *in situ* environmental cell for water mapping in PEMFC membrane electrode assembly (MEA) under controlled (T, RH) [32, 33]; and design, construction and commissioning of a cryo-STXM [34, 35] with the significant financial support of AFCC. Cryo-STXM is a promising platform to improve 3D mapping accuracy by significantly reducing radiation damage rates [36]. Other groups who have used soft X-ray SXM methods to study PEMFC materials and devices include Bozzini et al. [37–41], Ohigashi et al. [42] and George et al. [43]. While this chapter focuses specifically on applications of SXM to PEMFC, SXM is a broad range of instruments and methods, which can be applied to many areas of science and technology. Jacobsen [44] has recently published a comprehensive book on X-ray microscopy, which provides an in-depth coverage of principles, instrumentation, analysis methods and applications of both soft and hard X-ray microscopy techniques. In the last decade, reviews of SXM have been reported by de Groot et al. [45], Hitchcock [8, 9] and Braun et al. [46].

Of course, many other powerful analytical methods are available and provide competitive and/or complementary capabilities. Some of these methods are presented in detail in other chapters, such as Jankovic et al. (Microstructural and Spectroscopic Characterization of PEMFCs, Chapter 2), Cullen et al. (Characterization methods for Atomically-Dispersed Platinum Group Metal-Free Catalysts, Chapter 3) and Bazylak et al. (Synchrotron X-ray imaging of PEMFCs, Chapter 4). In order to place the SXM studies described in this chapter in a broader context of advanced analysis of PEMFC, a number of these methods are listed here, with references to recent studies, which

relate to the main subject of this chapter. Where appropriate, more details of alternate techniques are given in later sections describing SXM studies.

The closest equivalent to SXM is electron energy loss spectromicroscopy (EELS) in a transmission electron microscope (TEM). The energy resolution of modern TEM-EELS is quite similar to that achieved in synchrotron-based X-ray absorption spectroscopy and SXM. TEM has far better spatial resolution than SXM, and it has been shown that for very thin samples, molecular imaging can be done at lower radiation dose in electron microscopy than X-ray microscopy [47]. However, for analytical measurements involving TEM-EELS or X-ray fluorescence by energy dispersive spectroscopy (TEM-EDS), there is a significant advantage for SXM. TEM-EELS has considerable challenges for analytical studies of highly radiation sensitive PEMFC components such as PFSA or other ionomers. Several direct comparisons of SXM and TEM-EELS in terms of radiation damage per unit of analytical, core level excitation signal ("G-factor") have concluded there is a 100–500 fold advantage of SXM over TEM-EELS [48, 49], which is mostly related to the fact that the absorption of each X-ray photon at an analytically useful photon energy provides useful information while the vast majority of inelastic electron scattering events involve valence electron ionization, which cause bond breaking and damage, without providing analytically-useful core loss signal. Similarly, direct comparisons of SXM spectromicroscopy and TEM-EDS of ionomer in PEMFC cathodes have shown an enormous advantage for SXM [50]. Despite the analytical challenges, there are many excellent examples of electron microscopy—both secondary electron microscopy (SEM) and TEM—applied to PEMFC materials and systems [51–53]. Electron tomography (ET) has also been applied to PEMFC [54]. Discussion of the relative ability of TEM versus SXM to map ionomer in PEMFC electrodes is given elsewhere in this chapter. Another method very closely related to soft X-ray SXM is hard X-ray spectromicroscopy. The many variants of synchrotron based hard X-ray microscopy applied to materials research have been presented by Holt et al. [55]. Several groups have studied PEMFC devices under normal operating conditions [56–58], including the use of tomography [59] and laminography [60–62] for 3D mapping of water or Pt Lab-based hard X-ray tomography has also been used to study the 3D structure of operating fuel cells [63, 64].

This chapter is organized as follows. Section 5.2 describes SXM methods, including standard 2D-projection STXM; the application of STXM to mapping ionomer in PEMFC electrodes and MEAs; radiation damage monitoring and mitigation; 3D chemical mapping by tilt-series tomography and ptychography. The application of these methods to PEMFC issues is discussed as the methods are presented. Section 5.3 presents several specific applications of SXM to PEMFC, including optimization of distributions of ionomer in the cathode layer and STXM studies related to PEMFC degradation mechanisms, specifically Pt migration and carbon corrosion. Section 5.4 identifies future directions for SXM studies of PEMFC. Use of cryogenic STXM to reduce the radiation damage rate promises to allow more detailed studies of the 2D and 3D structure of ionomer in MEA electrodes. First steps toward *in situ* and *operando* studies of MEA under conditions close to operational are also described.

## 5.2 Methods

### 5.2.1 STXM instrumentation and methods

Figure 1a is a not-to-scale cartoon of the spectromicroscopy (SM) beamline at the Canadian Light Source (CLS) [65, 66] and interferometrically controlled STXM [67] including (from upper left to lower right): the elliptically polarizing undulator (EPU), which allows full control of the photon polarization (left/right circular and linear in any spatial orientation) [68]; some of the beamline optics (plane grating monochromator (PGM) to disperse the X-ray energies, and the exit slit, which is used to control coherence, energy resolution and incident flux; the M1 and M3 mirrors before and after the PGM are not shown) and the key STXM microscope elements—the Fresnel zone plate (ZP), order sorting aperture (OSA), sample and detector. To give a sense of the spatial distortion in Figure 1a, the distance from the source point (center of the EPU) to the sample in the ambient STXM is 33 meter [65] while the typical focal length of the STXM (ZP to sample) at the C 1s edge (300 eV) is 1 millimeter. Figure 1b is a photograph of the sample region showing (left to right): the aluminum snout of the UHV beamline, the brass carrier for the ZP, the OSA (laser drilled aperture in a piece of Mo foil) and the sample (Figure 1c, d), which, in this photograph, is a tomography system [21] consisting of a stepping motor for tilt angle rotation mounted on a standard trapezoidal aluminum STXM sample support plate [67]. The actual sample is a microtomed PEMFC-MEA supported on a formvar film, on a strip cut out of a 3 mm TEM Cu grid, as shown in Figure 1d. Figure 1e is a cartoon of how a STXM can be adapted to perform ptychography by adding a high-performance X-ray camera downstream of the sample to record the bright field and coherent scattered signal. More details on ptychography are given in a later section.

STXM is a complex, high precision, multiaxis mechanical device, which uses differential interferometry to monitor and control the (x, y) position of the sample with respect to the zone plate (ZP), and thus the X-ray beam. A full description of the microscope technology is given elsewhere [67]. Using typical high performance ZPs for focusing, a spot size of 20–30 nm is routinely achieved at most of the ~20 soft X-ray STXMs around the world (a complete list of all soft X-ray microscopes is available at http://unicorn.mcmaster.ca/xrm-biblio/xrm_bib.html). In 2020, the Swiss Light Source facility reported development of zone plates and associated improvements to the mechanical stability of the STXM, which allow them to routinely achieve 7 nm spatial resolution [69]. The photon energy range and ability to control the X-ray polarization depend on the source (bend magnet (BM), linear insertion device (ID) or EPU) and monochromator design (plane grating monochromator (PGM) or spherical grating monochromator (SGM)), and thus vary considerably among different soft X-ray STXMs. At the CLS-SM beamline, the EPU has four adjustable quadrants which provide: (i) fully linear polarized light with the linear E-vector orientation adjustable over 180 ° over the full photon energy range (130–3000 eV); (ii) fully circular polarized light over the EPU first har-
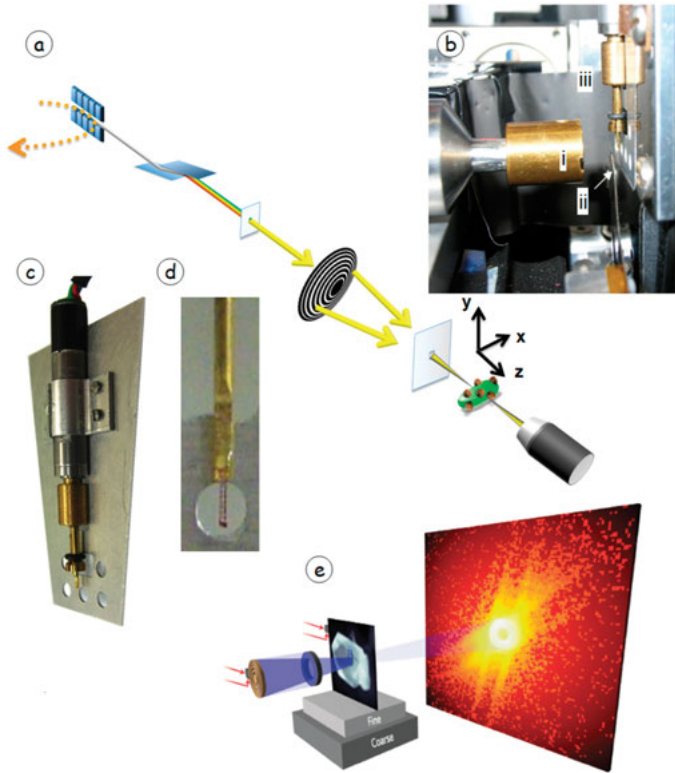
**Figure 1:** Schematic of a soft X-ray synchrotron beam line, and instrumentation for scanning transmission X-ray microscopy (STXM) and ptychography. (a) Cartoon of a typical soft X-ray synchrotron beamline and scanning transmission X-ray microscope (STXM). See text for details. (b) photograph of the sample region showing (i) the zone plate holder, (ii) order-sorting aperture, (iii) tomography sample. (c) photograph of a sample plate with stepper motor rotation stage [21] for tilt-angle tomography. (d) close-up of a grid strip as used for tomography. The formvar coating on the Cu grid supports an ultramicrotomed thin section of a membrane electrode assembly (MEA) of a polymer electrode membrane fuel cell (PEMFC). (e) Schematic of ptychography adaptation of STXM in which the phosphor-photo-multiplier integrating single channel detector is replaced by a high sensitivity X-ray camera in order to record coherent scattering patterns at each point in an (x, y) raster scan.

monic (130–1000 eV) and (iii) elliptical polarized light with variable circular/linear content above 1000 eV.

Detailed instrument description and operating procedures are published elsewhere [8, 67]. Briefly, after beamline tuning, instrument alignment, and sample focusing, the STXM is used to record transmission images at a single energy, to measure linescan spectra (intensity along a line at many photon energies), X-ray absorption spectra (XAS) at a single or multiple points and image sequences, also called stacks [70]. Imaging is typically performed by raster scanning the (x, y) positions of the sample when its z position is at the focal point of the X-rays. There are now several systems in which the ZP rather

than the sample is scanned, which allows for faster scanning and heavier, more complex sample environments. Spectroscopy and chemical mapping are best done using stacks, since this allows the user to accurately align images post-acquisition. After alignment, typical stack processing involves converting the as-recorded transmission signal to optical density, $OD = -\ln(I/I_0)$, using an $I_0$ signal either measured as part of the stack, or recorded separately before or after the stack. The OD stack, which could include one or more core level XAS signals, can be further analyzed using multivariate statistical analysis methods [71, 72], or forward fitting with suitable reference spectra [8] to derive maps for the chemical species present in the region of the sample measured. High quality X-ray absorption spectra [73] of a variety of PFSA materials from different vendors have been measured in STXM and analyzed in detail to provide a base for understanding the links between ionomer morphology (specifically, short side chain, versus Nafion™ species) and developing efficient ionomer mapping techniques. Figure 2, which is discussed in detail in the next section, gives an example of STXM images and spectra relevant to mapping ionomer in PEMFC-MEA electrodes. These basic STXM functions can be combined with systematic scans of other parameters such as linear or circular photon polarization, sample polar tilt angle (for tomography or dichroism mapping), sample azimuthal angle (for laminography or dichroism mapping), voltage (*operando* studies), time (kinetics and dynamics), temperature, humidity, etc.

## 5.2.2 Quantitative mapping of ionomer in catalyst layers

Reliable, quantitative high spatial resolution 2D and 3D distributions of PFSA ionomer in the catalyst layers (CL) of PEMFC membrane electrode assemblies (MEA) are critical for advancing understanding of the role of ionomer in PEMFC, and how it can be optimized [74]. This is an area where SXM methods excel, and thus it is a central theme of this chapter. Recording full range (40–60 eV wide), detailed (100–150 energy points per edge) stacks at all core levels of the system within the photon energy range of the beamline (e. g., S 2p, C 1s, N 1s, O 1s, F 1s, Pt 3d for the PEMFC system at CLS) does provide the most analytical information. However, this is often not practical, either due to beamtime limitations, or more typically, radiation damage limitations. At 50 nm point spacing, a stack measuring at 100 photon energies, using a sampling time per pixel of 1 ms takes ~40 min/µm$^2$). Under normal flux (10–20 MHz) and full zone plate focusing (30 nm spot), PFSA suffers 30 % damage (F mass loss and chemical structure modifications) in about 100 ms [28]. Ways to maximize useful analytical information with a given radiation dose are explored in several sections of this chapter.

After performing enough detailed studies to identify the chemical species present, and their key spectral features, it is usually advantageous, from the perspectives of both time efficiency and to minimize radiation damage artifacts, to use a reduced set of photon energies which can provide the analytical information essential for a given project. In the case of analysis of PFSA ionomer in MEA cathodes, Figure 2 outlines a strategy of
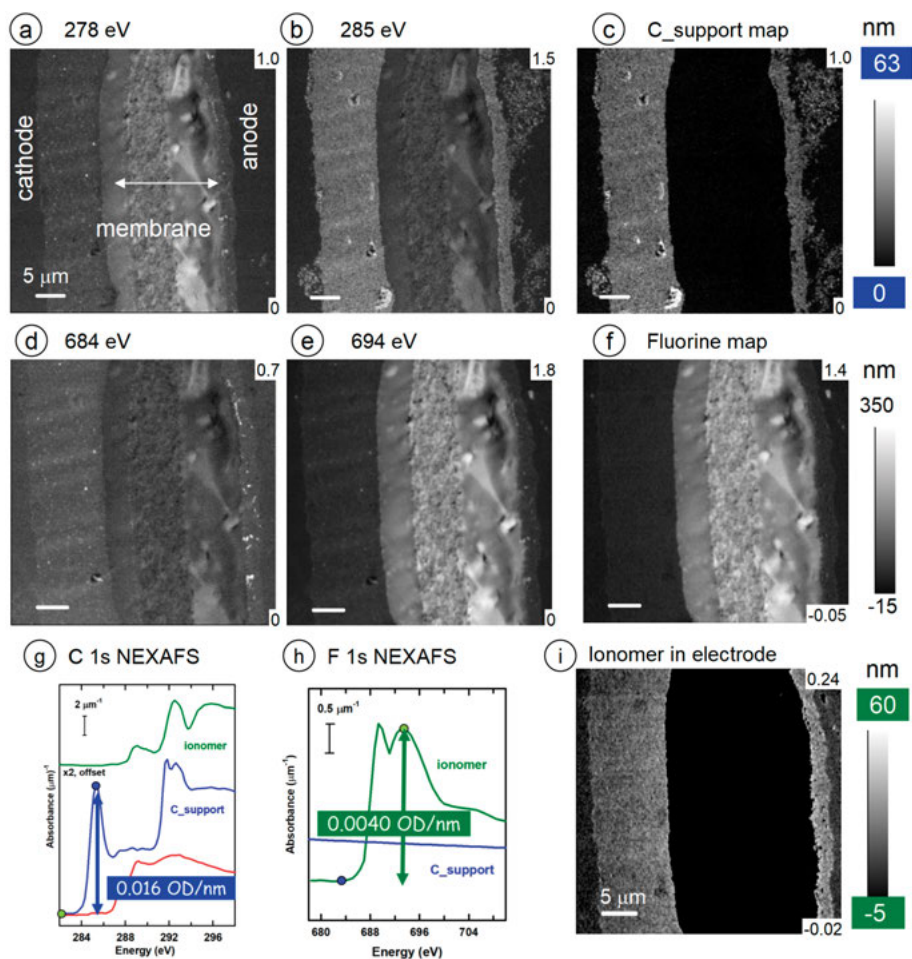
**Figure 2:** Quantitative, low-dose 2D mapping of ionomer in catalyst layers (CL) of a membrane electrode assembly (MEA) of a polymer-electrolyte membrane fuel cell (PEMFC) [10, 11]. Optical density (OD) images of an ultra-microtomed MEA extracted from a C 1s stack at (a) 278 eV and (b) 285 eV. (c) is the difference ($OD_{285} - OD_{278}$), which maps the carbon support (C_support) component. OD images from the F 1s stack at (d) 684 eV and (e) 694 eV. The numbers at the lower and upper right of each image are the limits of the OD grayscale. (f) is the difference ($OD_{694} - OD_{684}$) which maps the fluorinated regions, dominated by the membrane. (i) is the F-map derived by multiplying image (f) by a 0/1 mask with the threshold set to an OD intermediate between that of the membrane and that of the cathode/anode. (g) is the C 1s OD1 (optical density per nm) spectra of the PFSA, C_support and epoxy components. (h) is the F 1s OD1 spectra of the PFSA and C_support/ epoxy components. The difference in OD/nm indicated in (g) and (h) was used to convert the ΔOD scales in (c), (f) and (i) to an absolute thickness scale.

using only 4 specific photon energies to quantitatively map the PFSA ionomer relative to the carbon support. Figure 2 presents the images (Figures 2a, 2b, 2d, 2e), derived component maps (Figures 2c, 2f, 2i), and spectral basis (Figure 2g, 2h) for quantitative mapping

of ionomer in PEMFC- MEA. The 4-energy approach to qualitatively map carbon support (C_support) and ionomer was first reported by Susac et al. [10], while a later publication [15] presented the method for using the same four energy images to quantify C support, ionomer and Pt. In principle, depending on the chemistry, and thus spectroscopy of the material used for embedding microtomed samples, adding a 5th energy would provide unambiguous, quantitative mapping of the embedding media, which is a reasonable surrogate for the porosity [24]. The key to successful few-energy stack map approaches is identifying photon energies where the absorption signal for each component dominates. Generic, non edge-specific contributions can then be subtracted by taking the difference of images at the species-specific and non edge-specific energies. For MEAs, the C_ support component is mapped at the C 1s edge by [OD(285.1 eV) – OD(278 eV)] (Figure 2c, 2g) (or [OD(284.4 eV) – OD(278 eV)] if polystyrene (PS) is used to hold the MEA during microtoming). The membrane and the PFSA ionomer are mapped at the F 1s edge by [OD(694 eV) – OD(684 eV)] (Figure 2f, 2i). Since the membrane is 100 % PFSA, in order to visualize the ionomer in the electrodes it is necessary to use a threshold masking method to identify the pixels in the membrane, which are then set to zero (Figure 2i). Since the absolute OD1 response (optical density per nm) of pure PFSA at the C 1s and F 1s edges is known (see Figure 2g and Figure 2h) [73], the ΔOD grayscale for each species can be converted to a thickness scale (see Figure 2c, 2f, 2h). In addition, by subtracting a scaled PFSA map from the pre-C1s image at 278 eV, an estimate of the quantitative distribution of Pt catalyst can be generated, as discussed in [16]. Finally, if there is negligible penetration of the embedding material into the cathode (which can be achieved with polystyrene sandwiching techniques), pores above ~50 nm can be seen directly. In contrast, if a fully penetrating resin such as that made by reacting trimethylolpropane triglycidyl ether and 4,4′-methylenebis(2-methyl-cyclo-hexylamine) (referred to as TTE resin) [75] is used, the resin can be mapped (e. g., at the N 1s edge) and the resin map used as a quantitative map of the porosity [24].

The ability of this method to map ionomer in CL is an important advantage of STXM in the context of analytical methods for PEMFC. There are many publications that report use of analytical electron microscopy methods for qualitative and/or quantitative mapping of ionomer in CL using high resolution imaging [76, 77], X-ray fluorescence (TEM-EDS) [77], STEM-EELS [52, 77], electron tomography [78, 79] or staining techniques [80]. Melo et al. [50] directly compared F-loss rates as a function of X-ray exposure in STXM versus electron beam-based TEM-EDS mapping of ionomer in MEA cathodes, clearly showing the significant advantage of STXM relative to TEM-EDS. Yakovlev et al. [81, 82] have carefully reviewed the case for use of electron beam methods for quantitative high resolution mapping of ionomer in CL and concluded that reliable, damage-free results can only be obtained if the spatial resolution is drastically reduced. Due to the rapid damage of the ionomer [50] by both electron [26] and ion [27] beams, results from focused ion beam, secondary electron microscopy (FIB-SEM) methods to map catalyst layer microstructure in 3D [83–85] should be treated with caution. Based on our comparisons of relative damage rates, models of transport and other properties of PEMFC cathodes,

which are based on porosity or ionomer distributions derived from electron and ion beam methods [86, 87], may be flawed.

### 5.2.3 Radiation damage

In order to use STXM in a quantitative manner without artifacts associated with radiation damage, it is useful to estimate the radiation dose (in MGy, where $1\,\text{Gy} = 1\,\text{J/g}$) delivered in a given STXM analytical measurement and compare that to quantitative measurements of radiation damage as a function of dose. A systematic method to measuring both radiation damage and dose in STXM has been developed [88–90] and used to investigate X-ray damage of several polymer thin films, including polyethylene terephthalate (PET) [91], polymethyl-methacrylate (PMMA) [92] and PFSA ionomer [28]. Figure 3 presents OD images of a PFSA thin film before (Figure 3a) and after (Figure 3b) using the STXM beam to generate a 9-pad pattern by irradiating an initially uniform area of PFSA with controlled, systematically increasing doses. Figure 3c–3f compare C 1s, F 1s, O 1s and S 2p spectra of undamaged PFSA to those of the 3rd, 7th and 9th damage pad. At each edge, there is a systematic decrease in the intensity of the spectral features associated with intact PFSA (pre-C1s intensity; peaks at 173, 182, 292, 296, 690, 694 eV, the O 1s and F 1s continua) and a corresponding increase in spectral features associated with radiation damage products (C=C and C=O related peaks at 285, 287, 289 and 532 eV). Detailed analysis of the intensities of these features is used to derive critical doses for specific processes [28], which can be used to guide low-damage acquisition strategies.

In general, radiation damage by soft X-rays is found to obey first order kinetics [93]. Ideally, the dose used should be less than 20 % of the critical dose for any damage process (mass loss, electronic structure change, etc.) that would interfere with a quantitative analysis. The dose delivered by soft X-ray absorption can be calculated from the experimental conditions using

$$D = \frac{6.4 \times 10^5 \cdot E \cdot \text{OD1}(E) \cdot I_o\left(1 - e^{-\text{OD}(E)}\right) \cdot t}{K \cdot \pi \cdot s^2 \cdot \rho} \tag{1}$$

where $E$ is the photon energy (eV), OD1($E$) is the optical density for absorption by 1 nm thickness at standard density at energy E, $I_o$ is the incident flux (photons/s), OD($E$) is the OD for the sample at $E$, $t$ is the length of time the absorption occurs (dwell time), $K$ is the detector efficiency, $s$ is the area of the X-ray beam at the sample and $\rho$ is the sample density [90–92]. In fact, in cases where radiation damage causes mass loss and/or modification of the sample chemistry, such changes need to be taken into account in determining the dose, as described by Berejnov et al. [94, 95]. Within the approximation of first-order kinetics, a critical dose for a given radiation damage process can be derived by measuring changes as a function of increasing dose in the optical density at a photon energy sensitive to the type of damage of interest. For example, the main
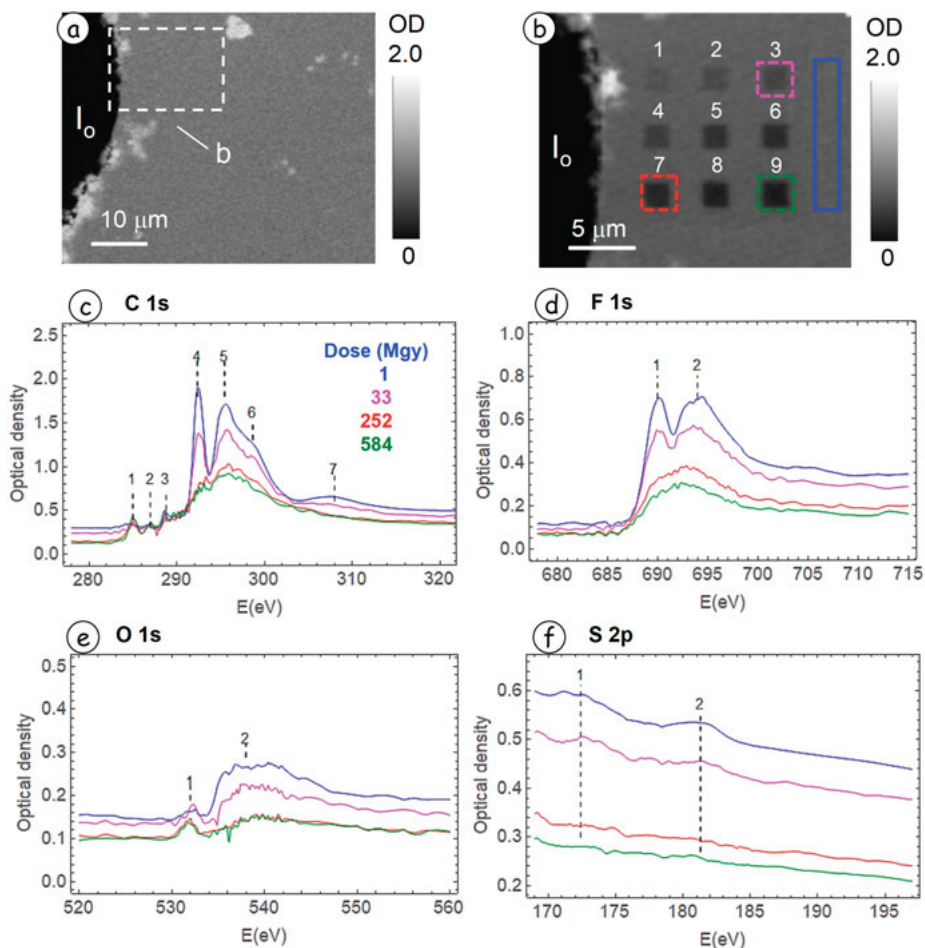
**Figure 3:** 9-pad pattern generation of radiation damage for quantitative understanding of radiation damage to perfluorosulfonic acid (PFSA) [28]. (a) STXM OD image of a spun cast thin film of PFSA on a silicon nitride support window, measured at 292.4 eV, before generation of a 9-pad radiation damage pattern. (b) STXM OD image at 690 eV of the 9-pad pattern generated at 320 eV in a He environment in the dashed rectangular area in (a). Io indicates the part of the image used for incident intensity measurement. Numbers denote the pad index. The near edge X-ray absorption (NEXAFS) spectra of the nondamaged area, blue (dose < 1 MGy); pad 3, pink (33 MGy dose); pad 7, red (252 MGy); and pad 9, green (584 MGy); are presented at the (c) C 1s, (d) F 1s, (e) O 1s and (f) S 2p edges. The color coding in the spectral plots identifying the pads corresponds to that in (b).

types of soft X-ray damage to PFSA are fluorine mass loss, ether-loss, sulfonate loss and degradation of the $-CF_2-CF_2-$ chain segments characteristic of the teflon™ backbone. The F-loss can be monitored at 280 eV (below C 1s) or from the difference in OD(710 eV) (F 1s continuum) and OD(680 eV) (pre-F1s). The sulfonate loss can be monitored at the S 2p edge (170–190 eV). The chain degradation can be monitored at characteristic C–F

bonding peaks at the C 1s edge [OD(292 eV), and OD(296 eV)] or the F 1s edge [OD(690 eV), OD(694 eV)]. We have found it very useful to make systematic 9-pad patterns (as displayed in Figure 3) using the Pattern Generation function of the STXM control software, which then allows to track the changes in full spectra, or the OD at specific photon energies as a function of increasing dose [28, 90]. Fitting that data to a first-order kinetic model can then be used to derive a critical dose [28]. Starting with undamaged PFSA, the critical dose for F-loss and chain degradation is $80 \pm 20$ MGy while that for sulfonate loss is somewhat lower ($50 \pm 20$ MGy).

Another aspect of STXM-based studies of X-ray damage is that the chemical changes induced by X-rays are similar to those resulting from electrochemical degradation of PFSA in PEMFC [29, 96]. Therefore, comparisons of materials degradation by chemical attack, such as through Fenton mechanism ($Fe^{2+}$ and hydrogen peroxide) [97, 98] caused by operation of a PEMFC and X-ray damage [19, 29] can give insights into PEMFC degradation chemistry.

## 5.2.4 4D imaging—spectrotomography of PEMFC cathodes

The 3D distribution of the components in CLs, in particular in the cathode where the rate limiting oxygen reduction reaction (ORR) occurs, determines porosity, and thus permeability and transport kinetics for fuels and products; electrochemical effectiveness, and thermomechanical properties. Section 5.2.2 described how detailed quantitative maps of the C_support, ionomer, Pt catalyst and porosity could be determined by either full-range stacks at the C 1s and F 1s edges, or by 4-energy stack maps, which minimize radiation damage. In the soft X-ray regime, tilt angle STXM tomography at multiple photon energies was first demonstrated in 2006 by Johansson et al. [99], and first applied to PEMFC cathodes in 2013 [20]. However, when typical tilt angle series sampling 50 or more tilt angles is used with a fully focused spot size, there is a large radiation dose (>300 MGy), and thus extensive sample damage. At that large a dose, there are serious questions as to whether or not the measured 3D spatial distributions of ionomer have any relationship to that in the undamaged cathode. Working with Paul Midgley and his group (Cambridge) and Mirna Lerotic (Second Look Consulting, Hong Kong), we developed and tested a new procedure for STXM tomography reconstruction [22], based on the total variation principle [100] applied to cone beam tilt-angle tomography, which is a type of compressive sensing (CS). CS can provide high quality 3D spatial distributions from quite small numbers of tilt angles (as few as 10) and limited tilt angle ranges ($\pm 50°$). The CS results were demonstrated to be as good as results from treating data sets from the same sample, which had a much larger number of tilt angles and larger angle range, but reconstructed using the serial iterative reconstruction technique (SIRT) or Fourier back projection [22]. This greatly improved reconstruction method allowed us to reduce the dose significantly. When we combined reduced tilt angles (14–16 angles are now typically used), with a reduced incident intensity (2 MHz rather than 20 MHz)

and defocusing the spot size from 30 to 50 nm, the overall dose for a 4-energy 2-edge stack map tomography tilt series was reduced from >300 MGy, to less than 15 MGy.

In order to evaluate the impact of radiation damage on 3D spatial distributions, we developed a multiscan procedure in which the same volume was sampled 3 times in succession with 14 tilt angles in each tilt series. The angles were interleaved so all 42 tilt angles could be used if desired. Figure 4 compares results from two, 3-pass spectro-tomography procedures, with different radiation dose and dose rates [23]. For the first measurement (Figure 4a–4d), full focus, large flux and a larger number of tilt angles (48) were used. The average F 1s spectrum of the whole cathode was measured before the start and after the finish of the 3-set measurement. The spectroscopy showed that about 40 % of the fluorine was lost, and all the remaining "PFSA" was transformed, as indicated by the disappearance of the characteristic double peaked structure (Figure 4d). The surface rendered face-on display of the reconstructed F-maps from the 1st, 2nd and 3rd set shows considerable modification of the spatial distribution.

In the second set (Figure 4e–4h), a lower dose rate, achieved by reducing the flux and using a slightly defocused X-ray beam, and fewer tilt angles (42) were used. The F 1s spectrum was measured 5 times, before the start, $\frac{1}{2}$ way through the first set, after the second set and finally after the third set of 14 tilt-angle, 2-energy acquisition. A defocused beam was used to get an averaged F 1s spectrum of the cathode, so negligible additional dose was imparted by these diagnostic measurements. In this case, due to the significant decrease in dose, there was relatively little change in the spectral shape and less than 10 % F loss (Figure 4h), even after all 3 sets of tilt-angle measurements. Figure 4e, 4f and 4g are slices through the center of the reconstructed volume. In this case, there is very little change in the spatial distribution with successive sets. These results are consistent with the estimated doses (a factor of ~10 less for the results shown in Figure 4(e–h) than those in Figure 4(a–d)). As summarized in Figure 4, the volume fraction of PFSA changes very little, reducing to 28 % from 31 vol% over the three tomography data sets. A movie of the 3D renderings of the second tomography data set shown in Figure 4 is available as supplemental material to ref. [23].

In addition to showing a rendering of the 3D structure of the PFSA from each of the 3 sets, the differences (set 2 – set 1) and (set 3 – set 2) are also displayed in the movie (see supplemental information of ref. [23]), which provides information about the location of the fluorine mass loss. Even with only 11 MGy total dose it is clear that thinner regions of PFSA are more susceptible to fluorine loss than thicker regions.

## 5.2.5 Pushing spatial resolution—ptychography

The improved acquisition methods that respect the radiation damage limits described in the last section have shown the feasibility of STXM tomography. However, the need for partial X-ray transmission, combined with high absorption cross-sections at the chemically specific energies, means that, for samples with a density of 0.5–2 g cm$^{-3}$, the thick-
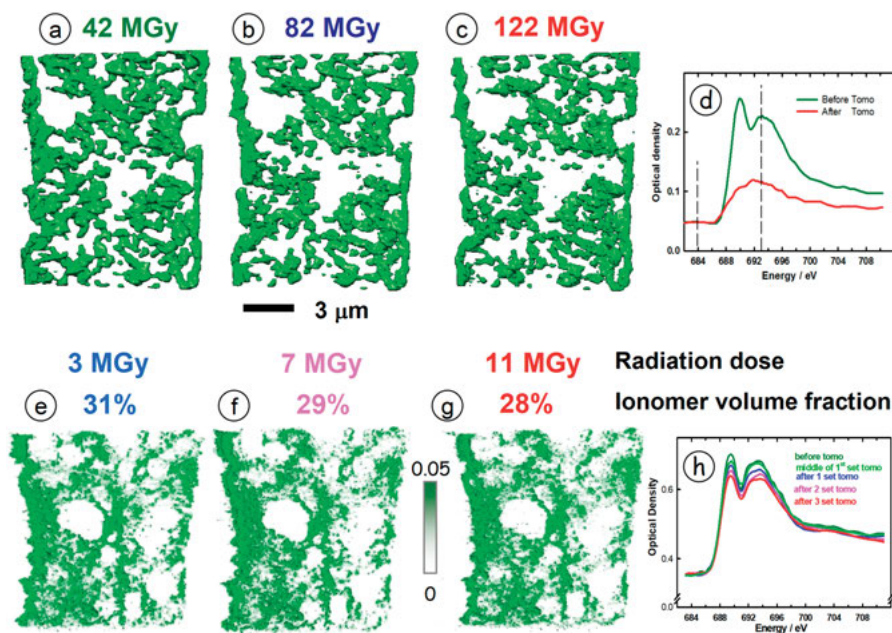
**Figure 4:** Use of multiset measurements to achieve ambient STXM three-dimensional (3D) mapping of ionomer in cathode layers with minimal radiation damage [23]. (a), (b), (c) Surface rendered 3D maps of PFSA in a PEMFC cathode, derived from a compressed sensing (CS) reconstruction of two energy F 1s spectrotomographic measurements. Three successive 16 tilt angle data sets (each consisting of STXM images at 684 eV and 705 eV) were recorded from the same volume, with integrated radiation doses of 42, 82 and 122 MGy for sets 1, 2 and 3. (d) Average F 1s spectra of the cathode prior to the first tomography measurement and after the end of all 3 measurements. (e), (f), (g) slices from the 3D distribution of the PFSA in a PEMFC cathode derived from CS reconstruction of two-energy F 1s spectrotomographic measurements of three, 14 tilt angle data sets on the same volume. By using fewer tilt angles, much lower incident flux, and a small defocus (increasing the spot size from 30 to 50 nm), the integrated radiation doses after each set were only 3, 7 and 11 MGy. The change in the average volume fraction of ionomer after each tilt series is indicated, amounting to about 10 % F-loss over the full data set. The intensity scale bar is voxel OD in a thickness of 10 nm. (h) Average F 1s spectra of the cathode, before measurements, at the middle of first tomography scan, and after the 1st, 2nd and 3rd tomography data sets.

est slices that can be measured by soft X-ray tilt series tomography are about 300 nm. With a 3D resolution of ~50 nm the information in the third dimension is limited to at most 6 discrete resolution elements. In addition, at high tilt angles the actual path length through a planar sample is 2–3 times larger than the sample thickness, which leads to artifacts associated with absorption saturation. The latter problem can be significantly reduced by use of laminography rather than tilt angle tomography. An apparatus optimized for soft X-ray STXM laminography measurements of planar samples has recently been commissioned at the PolLux beamline at the Swiss Light Source [101].

An approach to enhance 3D information is to improve the spatial resolution. The spatial resolution in zone plate-based STXMs is limited by the properties of the ZP. With

highly coherent illumination, the diffraction limited resolution is $1.22 \cdot \delta_r$ where $\delta_r$ is the width of the outermost zone of the ZP [44]. While a spatial resolution of less than 8 nm has been demonstrated [69], the zone plate used is inefficient and the focal length very short, such that it is very difficult to use. Recently, the spatial resolution limitation of ZP optics has been overcome through the use of ptychography, a coherent diffraction imaging (CDI) technique [102]. Ptychography uses the same type of raster scanning as conventional STXM. At each (x, y) point in the scan, a low background, high sensitivity X-ray camera positioned 4–10 cm after the sample is used to record the coherent diffraction pattern, including both the bright field annulus, which contains diffraction signal as well as undiffracted photons, and all of the X-rays coherently scattered by the sample, out to as large a scattering angle where the diffraction signal can be differentiated from background. Using appropriate software such as PyNX [103], SHARP [104] or Ptypy [105], the CDI pattern from each spot is reconstructed into a real space image. By using a point spacing where the points overlap (by 30–50 % if using a zone plate focused X-ray spot, or 80–90 % if using a defocused 0.5–1.0 µm spot), the constraint that the reconstruction of the CDI pattern at one spot gives the same result as that in the areas which are also measured in adjacent spots, leads to a rapid and reliable convergence of the iterative method used for reconstruction. Added benefits of ptychography include provision of (a) the phase and spatial distribution of the X-ray probe, which can help optimize instrumentation performance; (b) the phase as well as amplitude of scattering, which can be analyzed together simultaneously to enhance the reliability of chemical analysis, resulting in refraction-based spectromicroscopy [106]. Although a zone plate is used to produce a cone-beam X-ray source with spot size at the focal point of 40–100 nm diameter, ptychography is not limited by the ZP properties and thus has the potential to reach the Rayleigh limit dictated by the wavelength of X-rays used ($\lambda$(nm) = 1239.8/E(eV), thus ~4 nm at the C 1s edge). Recently, the COSMIC beamline and two microscopes dedicated to soft X-ray ptychography have been developed at the Advanced Light Source. The record spatial resolution, which was achieved using 1500 eV photons, is 3 nm [107]. In addition to providing the highest spatial resolution in the world in the soft X-ray range, COSMIC is extensively equipped for *in situ, operando* [108] and tomographic experiments [108, 109].

Results from the first application of soft X-ray ptychography to a PEMFC cathode [31] are presented in Figure 5. Figures 5a and 5b show absorption images (OD scale) from ptychography measurements at 684 eV and 694 eV. Figure 5c, the difference between Figure 5b and Figure 5a, maps the PFSA in both the catalyst layer and the membrane. Note that the dark regions in the fluorine map (Figure 5c) correspond to the bright regions in Figure 5a, which are carbon-rich. The PFSA ionomer in the catalyst layer (Figure 5c) has a "feather" morphology superimposed on a fine network structure. We believe the rather uniform "feathery" areas correspond to a film of ionomer smeared over the cathode during the room temperature microtomy. Figure 5d is a color-coded composite of the F-map and the carbon support, with the latter derived from the pre-F 1s image and the F-map (carbon support = $OD_{684}$ − 0.21 ∗ F-map). Figure 5e, an expansion of the PFSA
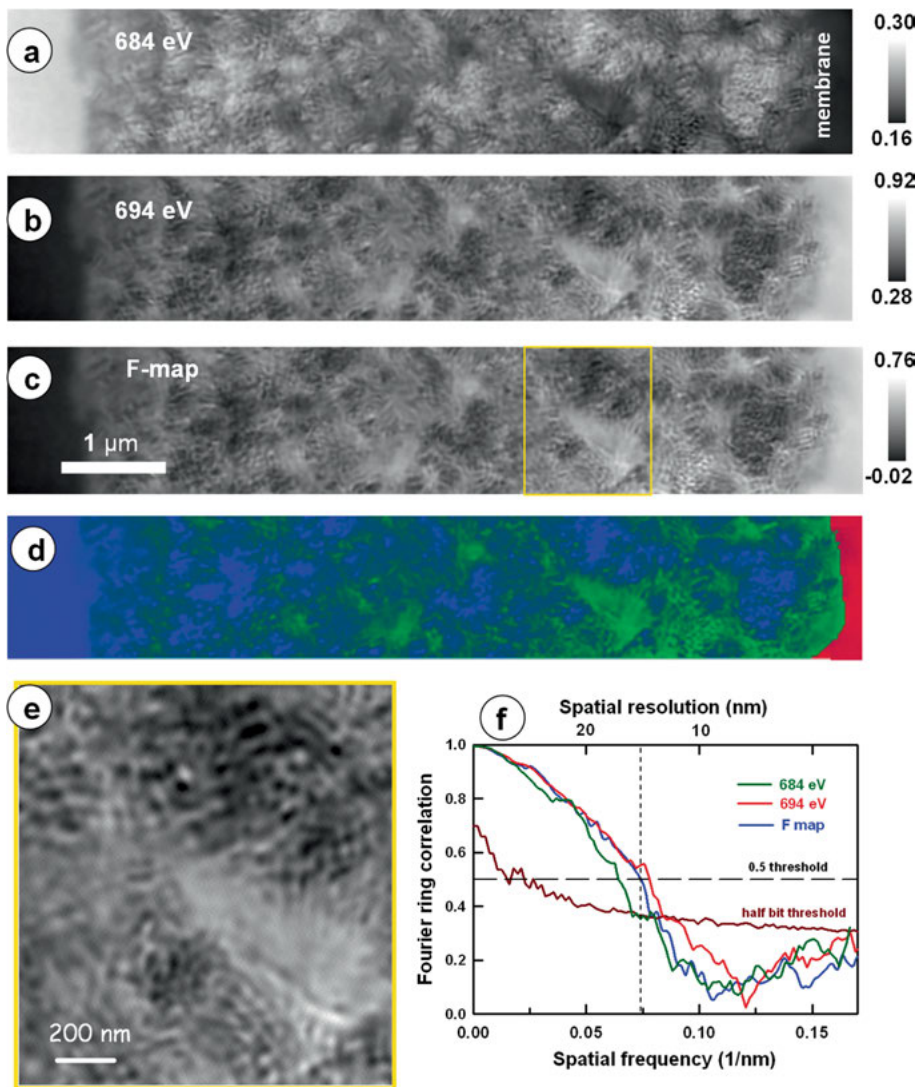
**Figure 5:** Improving spatial resolution of ionomer mapping in PEMFC MEAs by spectro-ptychography [31]. Ptychography-derived OD images of an MEA cathode at (a) 684 eV. (b) 694 eV. (c) difference (PFSA ionomer/membrane map). The optical density grayscale is indicated for each image. (d) Color-coded composite of the membrane (red), ionomer (green) and carbon (support & epoxy) (blue). The membrane and ionomer signals are derived from the total fluorine signal by threshold masking, and thus provide a quantitative map of the PFSA. The carbon signal is derived from the image at 684 eV [31]. (e) expansion of the PFSA map in the region of the yellow box in (c). (f) Fourier ring correlation (FRC) analysis of (c) indicating a spatial resolution of 15 nm. (adapted from Figures 5 and 6 of [31]; reproduced with permission from American Chemical Society, © 2018).

map in the region of the yellow box in Figure 5c, shows both the fine network structure and the "feathery" smear in greater detail. Fourier ring correlation (FRC) analysis (Figure 5f) of the PFSA map indicates a spatial resolution of ~15 nm. It is noteworthy that these results, recorded in 2015, in the early days of the development of ptychography at the ALS, were obtained with only 2 ptychographic measurements, each of which used only 20 ms to acquire the diffraction image at each spot. Including navigation set-up imaging and spot overlap, each area of the sample was exposed to only ~60 msec of beam with an estimated dose of 8 MGy, which is ~10 % of the critical dose for PFSA. COSMIC, a dedicated and highly optimized soft X-ray ptychography beamline at the ALS started operation on 2017. With its greater stability and higher coherent flux, it is possible to achieve <10 nm spatial resolution using 10 msec dwell per diffraction image [109]. Thus, 2D mapping of PFSA in PEMFC electrodes at sub-10 nm spatial resolution with negligible radiation damage is possible. Meaningful 3D ionomer distributions are also likely achievable since COSMIC Nanosurveyor 2 endstation is equipped for cryo-tomography. Using cryo conditions (sample $T$ below –200 °C) is known to greatly reduce the rate of mass loss radiation damage [110]. Recently, the cryo-STXM at the CLS [35] has been used to compare rates for chemical modification of PFSA by X-rays with the sample at –175 °C versus at 25 °C [36]. The preliminary results show that cryo-cooling to near liquid $N_2$ temperatures results in a substantial reduction in the rate of chemical modification, as well as preventing mass loss. This is in considerable contrast with polymethylmethacrylate (PMMA). STXM spectromicroscopy of X-ray damaged PMMA with the sample at –160 °C showed identical chemical damage rates as at 25 °C [110], an observation reproduced in the recent cryo-damage measurements [36].

## 5.3 Examples of STXM applications to PEMFC optimization

### 5.3.1 Optimization of ionomer distributions in CL

While the balance of Pt coated carbon particles, Pt loading and the amount of PFSA ionomer is known to be optimized with a weight percent of ~30–40 % of ionomer [111, 112], the reason for this optimum was not well understood prior to use of STXM as a probe of the spatial distributions of ionomer in CL. The ionomer imaging methods described in Section 5.2.2 were applied to several different CL preparations with two different catalyst supports and systematic variation in the ionomer loading. Figure 6 presents color-coded composites of the ionomer and carbon support spatial distributions for low surface area carbon (LSAC), and high surface area carbon (HSAC) supports with ionomer loadings of 10–13, 33 and 45 weight % [113]. At the lowest ionomer loading the distributions are relatively uniform, with an increasing amount of ionomer on the membrane
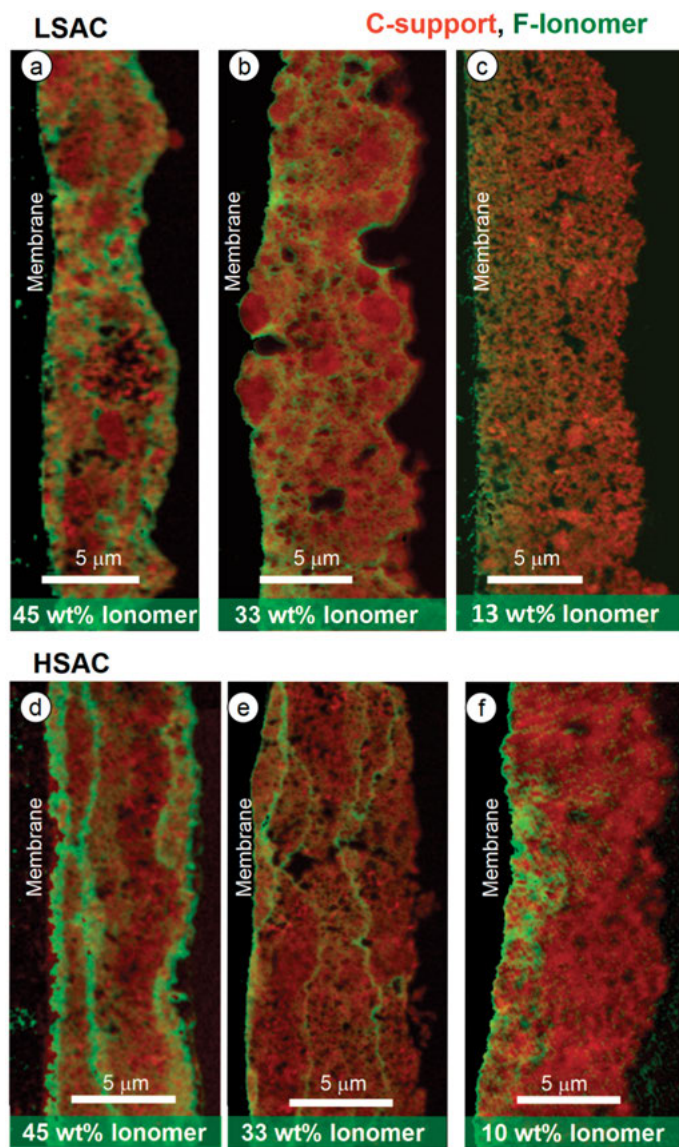
**Figure 6:** Use of STXM-based ionomer imaging to help understand optimization of catalyst ink composition by visualizing nonuniform ionomer distributions. (a)(b)(c) Carbon support (red) and ionomer (green) color composite maps derived from 4-energy (C 1s, F 1s) STXM measurements of PEMFC cathodes based on low surface area carbon (LSAC) carbon support, for formulations with (a) 45, (b) 33 and (c) 13 weight-% of ionomer in the catalyst ink. (d)(e)(f) Carbon support (red) and ionomer (green) color composite maps derived from 4-energy STXM measurements of PEMFC cathodes based on high surface area carbon (HSAC) carbon support, for formulations with (a) 45, (b) 33 and (c) 10 weight% of ionomer.

side. However, as the ionomer loading increases, the ionomer distribution becomes increasingly heterogeneous. For the LSAC support, there are characteristic ovoid regions of depleted ionomer content (Figure 6a, 6b) (similar ovoid structures are evident in the 3D mapping, see Figure 4 [23]). For the HSAC support, there are characteristic layered zones of high ionomer content, separated by ionomer depleted zones (Figure 6d, 6e). As the spatial distribution of ionomer gets less homogenous large portions of the CL will most likely underperform, due to reduced proton transport. Thus, the observation of an optimum ionomer loading of ~30 weight % is a consequence of having insufficient amounts of ionomer for adequate proton transport at low loadings, and too many "dead zones" with reduced gas access when the loading gets above 30 %. The heterogeneous distributions are most likely a consequence of partial phase separation in the catalyst inks during or after deposition, suggesting that improving the homogeneity and stability of catalyst inks would be an avenue to further optimize the CL structure.

## 5.3.2 PEMFC degradation mechanisms

A significant issue delaying commercial mass market implementation is achieving sufficient reliability, especially in personal automobiles where fuel cell stacks will experience a wider range of environments and operating conditions compared to for example stationary power applications. STXM has been used in several areas to investigate mechanisms of electrochemical performance degradation. Pt dissolution and migration, which can occur when there is cell reversal [114, 115], involves oxidation of Pt, migration of Pt ions from the CL into the membrane and then formation of metallic Pt deposits at the zone of zero charge [116, 117]. An interesting question is "*what aspects of the chemistry of the Pt in the CL might make the system more* (*or less*) *susceptible to Pt dissolution*"? When studying the Pt particles in the membrane in one system where the Pt catalyst was introduced by reducing a nitro-amine based Pt organometallic compound, STXM measurements showed there was a significant N 1s signal localized at the Pt particles [14]. Further, the N 1s NEXAFS spectrum of the particles was similar to that of the Pt particles in the cathode, but different from a weak N-containing signal (of unknown origin) in the membrane. Figure 7a–7c are component maps derived from N 1s stacks measured in an area of the membrane of an end-of-test sample with significant Pt migration. The analysis is based on fitting the N 1s stack to the N 1s spectra presented in Figure 7e and 7f. Figure 7d is a color-coded composite of the three component maps. When compared to the N 1s spectrum of the cathode (black curve in Figure 7d, 7e) the spectrum of the core of the Pt particles is very similar, suggesting that residual nitrogenous material from the nitro-amine based Pt precursor may have participated in, and perhaps facilitated migration of the Pt from the cathode into the membrane. N 1s STXM studies of Pt migration regions in an end-of-test CL where the Pt was derived from $PtCl_4$ did not show this N 1s signal, supporting the idea that the residual N from the amine ligand might be involved
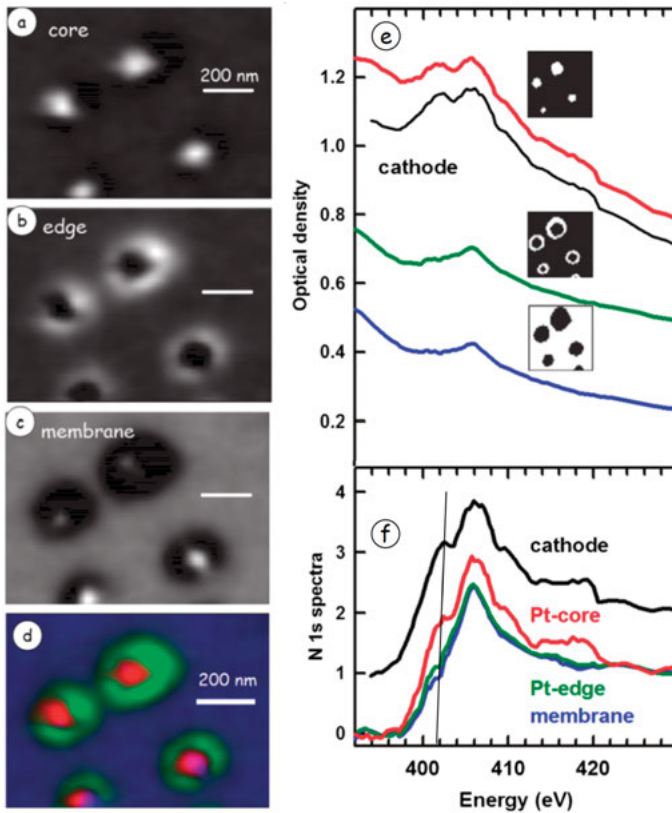
**Figure 7:** Example of a N 1s STXM study of degradation by Pt migration. (a–d) STXM spectromicroscopy: mapping an end-of-life PEMFC in the region of a Pt – in – membrane band at the N 1s edge [14]. (a) Component map of the Pt core, (b) component map of the signal at the edge of the particles, (c) component map of the membrane, (d) color coded composite of the three component maps. (e) Comparison of the N 1s spectra of the Pt core (red), compared to that of the cathode (black), the edge of Pt particles (green) and the membrane away from the particles (blue). The inset masks indicate the regions from which the spectra were obtained. (f) N 1s spectra of the membrane, Pt-edge, Pt-core and cathode after subtraction of a curved background extrapolated from the pre-N 1s region and unit normalization in the continuum. The spectrum of the cathode is offset by 1 unit (Reproduced from [14] with permission from the PCCP Owner Societies).

in Pt dissolution and migration. Unfortunately, both types of CL (with and without N) were found to be similarly susceptible to Pt dissolution [14].

A second important area of PEMFC degradation is that of carbon corrosion [118]. When PEMFCs are operated at high potentials as in start-up/shutdown conditions, the carbon black catalyst support is oxidized to $CO_2$. This can lead to performance decrease due to reduced catalyst surface area and/or alteration of pore morphology. A better understanding of the mechanism of carbon corrosion is needed to support rational design of mitigation strategies. One of the questions in this context is the extent to which the
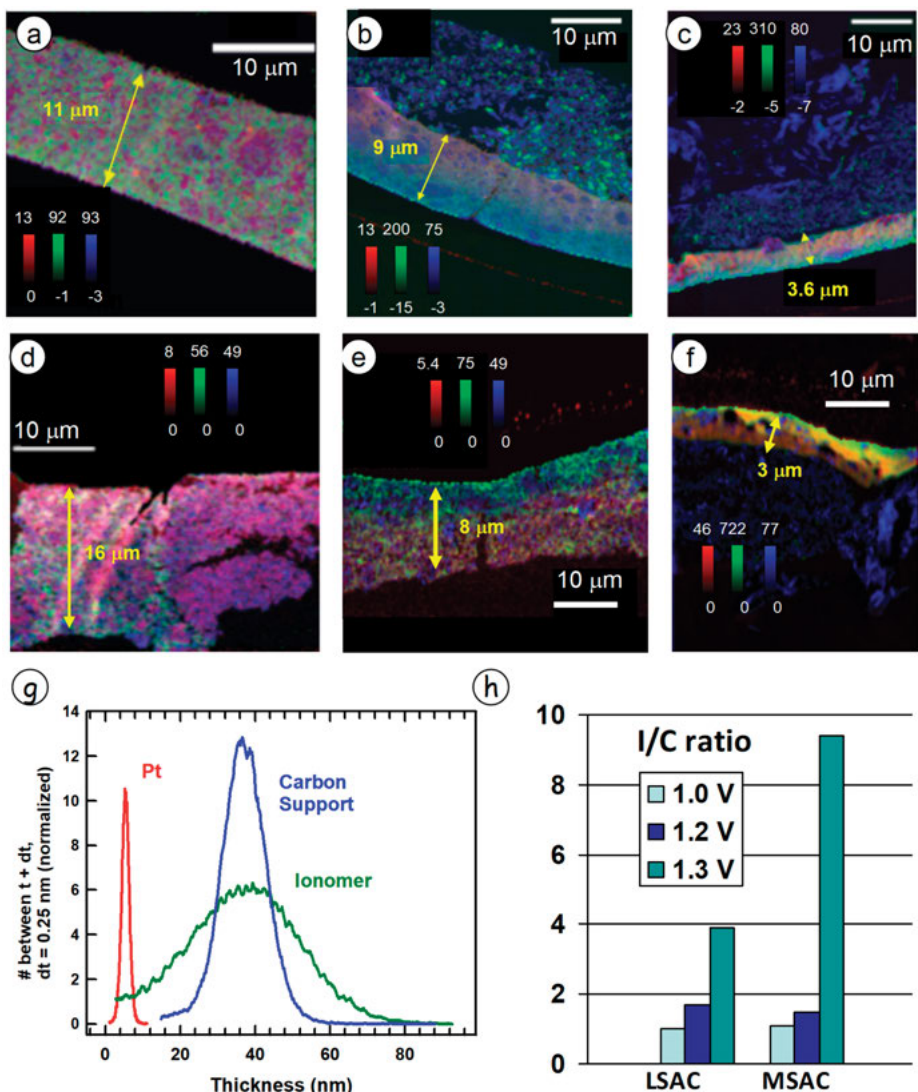
**Figure 8:** Carbon corrosion studied by STXM [15]. (a–f) are color coded composite maps of the thickness distributions (in nm) of Pt (red), ionomer (green) and carbon support (blue) in the cathode region of a PEMFC- MEA subjected to accelerated stress testing (end-of-test) with an upper voltage of 1.0 V (a, d), 1.2 V (b,e) and 1.3 V (c, f). The upper row (a–c) is from samples using a low surface area carbon (LSAC) support while the lower row (d–f) is from samples using a medium surface area carbon (MSAC) support. The membrane, which is on the smooth side of the cathode, and the embedding support, which shows particles in the microporous layer in some cases, have been removed by threshold masking (see Figure 2(f, i)). The dramatic shrinkage of the width of the cathode is due to carbon corrosion. (g) is an example of the histograms of the Pt, ionomer and carbon support thicknesses from (a). Similar quantitative results for all six samples were used to derive the ionomer to carbon support (I/C) ratios displayed as a bar graph in (h).

PFSA ionomer is lost or modified in extreme carbon corrosion events. In collaboration with scientists at Ballard Power Systems, STXM was used to study the chemical changes in the cathode CL in samples subjected to accelerated stress tests, consisting of many voltage cycles between 0 and $V_{max}$ where $V_{max}$ is between 1.0 and 1.3 V [15]. Figure 8 presents results from that study in the form of color-coded composites of the distributions of Pt, ionomer and carbon support in the cathodes of PEMFC samples, using LSAC (Figure 8a, b, c) and medium surface area carbon (MSAC) support (Figure 8d, e, f), which had been subjected to 1000s of electrochemical degradation cycles where the peak anodic potential was 1.0 V (Figure 8a, d), 1.2 V (Figure 8b, e) or 1.3 V (Figure 8c, f). Figure 8g is an example of the distribution of thicknesses of these components, extracted from the component maps of the cathode composition, in that case for the beginning of test (BOT) LSAC sample. Similar histograms were evaluated for the six samples and used to generate the ionomer to carbon (I/C) ratio, expressed as the mean of the ionomer thickness distribution divided by the mean of the carbon support thickness distribution. Figure 8h is a bar chart of the I/C ratio for the 6 end of test (EOT) samples. This study showed that the highly oxidative conditions caused extensive loss the carbon support, and the loss of carbon occurred to a similar extent with the LSAC and MSAC support [15]. However, there was relatively little loss of the ionomer, particularly in the MSAC samples, which then resulted in a large increase in the I/C ratio as the peak voltage increased. Further, measurements at the S 2p edge indicated that the sulfonate groups were largely resistant to the oxidative conditions causing the extensive carbon corrosion, implying that even after carbon loss, the ionomer could still be functional as a proton conductor [15].

# 5.4 Future directions for SXM studies of PEMFC

## 5.4.1 Low damage STXM of PEMFC MEAs

A lot of progress has been made over the past decade in evolving STXM techniques, which can measure 2D ionomer distributions with relatively little radiation damage induced changes in the fluorine levels, electronic structure or modification of the nanostructure [26, 90]. However, it is the 3D structure of the CLs, and how that may evolve under different operating conditions, that determines performance and stability. With few-angle acquisition methods and advanced tomographic reconstruction methods (see Section 5.2.4), it has been possible to measure 3D ionomer distributions at ambient temperature with a dose similar to that typically used in 2D measurements, although with somewhat reduced spatial resolution (50–80 nm in 3D versus 25–30 in 2D) [23]. Despite that technical achievement, only limited extents of 3D structure can be measured with conventional tilt-angle tomography due the strong absorption in the soft X-ray region, which limits samples to ~300 nm thickness and degrades 3D spatial resolution due to

out-of-focus conditions at high tilt angles. Laminography, in which the 3rd dimension is accessed by rotating the sample azimuthally [119], offers one route to providing more extensive 3D results since (i) much larger volumes can be accessed, (ii) the absorption is uniform at all azimuthal angles, and is smaller than at high tilt angles in tilt-angle tomography; (iii) the focus does not change with angle. Laminography using tunable hard X-rays in the region of the Pt $L_3$ edge has been applied to PEMFC [60, 61]. Recently, a practical system for soft X-ray laminography has been implemented in the STXM at the Swiss Light Source [101].

Another approach to measuring the 3D structure of radiation sensitive systems with reduced damage is measurements under cryogenic conditions. This approach is very common in studies of biological samples but has been used relatively infrequently in materials science. An open question with regard to cryogenic studies of ionomer in CL is the extent to which maintaining a sample near liquid $N_2$ temperature will reduce the rate of radiation damage. As noted earlier in this chapter, the damage mechanism, which occurs at low doses and causes extensive reorganization of the material, is C–F bond breaking combined with fluorine loss. Reducing mass loss by "freezing in," and thus retarding loss of low molecular weight damage fragments is an accepted benefit of measuring dense materials under cryo conditions. This mechanism may be less effective in preventing loss of radiation damaged ionomer due to the open pore structure of CL. Recently, we have used the cryo-STXM at the CLS [35] to measure rates of fluorine loss and electronic structure changes in PFSA at 25 °C and –170 °C [36]. We also measured the radiation damage and mass loss at the O 1s edge of polymethylmethacrylate (PMMA) under cryo conditions. The temperature dependence of radiation damage to PMMA was studied much earlier by Beetz and Jacobsen [110]. They showed that cryo conditions prevented mass loss but did not affect the rate of electronic structure modification, as monitored by the intensity of the O 1s $\rightarrow \pi^*_{C=O}$ transition at 532 eV. Our study [36] verified the earlier results on PMMA. Interestingly, both mass loss and electronic structure changes in PFSA, monitored at the F 1s $\rightarrow \sigma^*$ transition at 694 eV, proceeded at a much-reduced rate at –170 C as compared to 25 °C [36]. Although this observation holds promise for being able to improve the spatial resolution and signal quality of ionomer in CL measurements by using cryo-STXM, further study is needed, since there was significant ice build-up in those measurements, which could have played a role in reducing mass loss.

## 5.4.2 Progress toward *in situ* and operando studies of PEMFC by soft X-ray STXM

It is widely believed that significant improvements to PEMFC technologies are most likely to arise from operando studies [120–124] in which all or a subset of the PEMFC system is studied with spectromicroscopy methods under realistic operating conditions.

Issues which could be better understood with appropriate operando studies include optimization of water distributions [125, 126], low temperature modifications to CL structure ("cold start"), start-up/shut-down reversal induced Pt migration and carbon corrosion [61].

Several *operando* or *in situ* soft X-ray STXM studies of electrocatalyst systems have been carried out using soft X-ray STXM and ptychography. Lithium batteries [127–129], Zn-air batteries [130], supercapacitors [40] and half-cell ionic liquid based systems [41] are among the systems studied. However, so far a full-working PEMFC system has not yet been probed by soft X-ray microscopy, which is perhaps not surprising given: (i) the extremely tight spatial constraints (see Figure 1); (ii) the requirement for introducing/exhausting reactant gases, and product water, as well as controlled heating to the typical 80 °C operating temperature and (iii) the large X-ray absorption coefficients in the soft X-ray region. Custom STXM devices for variable T [131]; variable humidity (RH [132, 133]; simultaneous (T, RH) control [32, 33]; liquid flow [132, 134]; electrochemistry [135–137]; and combined fluid flow and electrochemistry [138] have been built and tested under near-operating conditions for a variety of scientific studies.

As an example of *in situ* STXM, Figure 9 presents results from a study of hydration of a microtomed slice of PEMFC MEA in a controlled humidity environmental cell. Figure 9a is a photo of an *in situ* cell with both (T,RH) feedback control [15] mounted in the CLS ambient STXM. A heating/cooling Peltier thermoelectric device and a thermocouple in good thermal contact with the sample are used to establish sample temperatures from −20 to +80 °C with feedback control. A humidity sensor in a flow of humidified He close to the sample is used to operate proportional valves in wet and dry He streams to maintain the user-selected humidity at the chosen operating temperature. One of the attractive aspects of the use of STXM for mapping water distributions in MEA is the ability of O 1s NEXAFS spectroscopy to easily differentiate the O 1s signal of PFSA and the gas, liquid and solid phases of water; see Figure 9b. Results from a study of liquid and gas distributions in a microtomed slice of an MEA at $T = 22$ C and RH = 85 % [32] are presented in Figure 9c–f. Figure 9c is an OD difference map ($OD_{694} − OD_{684}$) of the fluorine, and thus the ionomer, in both the electrodes and the membrane. The latter is a Gore SELECT® ePTFE micro-reinforced membrane, where the central third of the membrane is a highly porous reinforcement region. The ultramicrotomy preparation used a novel polystyrene (PS) sandwich embedding process where beads of PS softened by exposure to toluene vapor, press against the MEA to hold it in place for ultra-microtoming without the PS penetrating into the electrodes. Unfortunately, the cathode fragmented during the microtoming. Despite this, representative regions, free of embedding resin, were present and used for the humidification study. Figure 9d is an image at 540 eV, taken from an O 1s stack (524–564 eV, 60 energies) measured under high humidity conditions, The stack was fit to the O 1s spectra of PFSA, liquid and gaseous water, and a constant (for carbon and catalyst in the cathode). A color-coded composite of cathode, PFSA, and liquid water maps is presented in Figure 9e while the composite of the gaseous $H_2O$, PFSA and liquid $H_2O$ maps is presented in Figure 9f. As expected, gaseous water was found in the highly
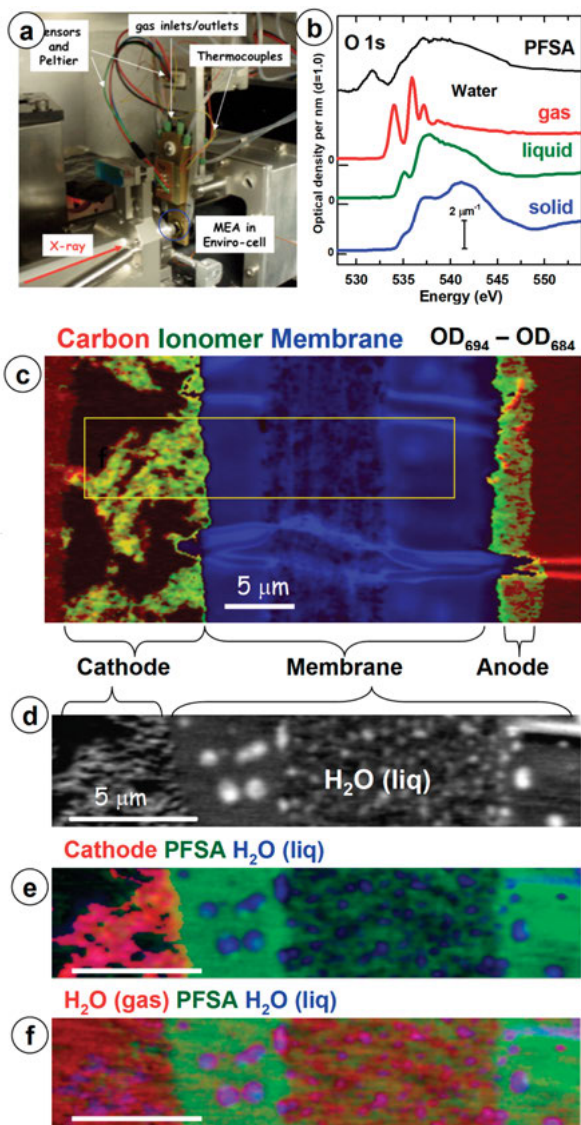
**Figure 9:** Example of an *in situ* STXM study of PEMFC MEA. (a) Photograph of the temperature and humidity (T,RH) controlled environment *in situ* STXM cell mounted in the polymer STXM on BL 5.3.2.2 at the Advanced Light Source. (b) O 1s spectra of gas, liquid and solid water. (c) Color-coded composite of component maps of the full width of an ultramicrotomed section of an MEA of a PEMFC derived from STXM OD images at 684 eV (pre-F1s) and 694 eV (F 1s maximum). The layers of the structure are labeled. The yellow rectangle indicates the area mapped under high RH conditions. (d) Component map of liquid water from fit of an O 1s stack recorded from the MEA in the environmental cell under saturated humidity conditions ($T = 25$ C, RH $= 85$ %). (e) Color-coded composite of component maps for cathode (no O 1s, red), PFSA (green) and liquid water (blue), derived by stack fit to the O 1s stack. (f) Color-coded composite of component maps for water vapor (red), PFSA (green) and liquid water (blue), derived by a fit of the O 1s stack to the O 1s spectra of PFSA, gas and liquid water, and a constant to map the carbon support in the cathode.

porous regions of the cathode and the e-PTFE micro-reinforced layer of the membrane. In contrast, rather than diffusing into the dense part of the membrane, the liquid water was observed as droplets on the surface of the dense regions of the membrane, filling the pores in the e-PTFE micro-reinforced layer, and the cathode (Figure 9d, 9f). The lack of penetration of liquid water into the membrane is most likely because the microtomed section was bone dry at the start of the experiment and not subjected to the peroxide conditioning typically used to activate membranes by making continuous hydrophilic pathways [139].

In general, operando STXM lags behind operando TEM [140] and operando hard X-ray [141, 142] capabilities, in both instrumentation and number of published studies. Hard X-ray synchrotron radiography [143] and lab-based hard X-ray tomography [63, 64] have been applied to study water distributions in full PEMFC using specialized thin cells with hard X-ray transparent windows. Such studies have provided useful insights into how liquid and vapor water distributions change under different operating conditions. However, it has been noted that radiation damage by hard X-rays, especially at the Pt L-edge, affects the operational electrochemical characteristics of the devices at a much faster rate than material damage [144, 145] probably due to hard X-rays being preferentially absorbed at the Pt catalyst resulting in modifications of the local structure and chemistry at the critical catalyst site.

## 5.5 Summary

Synchrotron radiation (SR) based scanning X-ray microscopy in the soft X-ray regime is a versatile tool for advanced chemical analysis and imaging of materials, devices and processes central to polymer electrolyte membrane fuel cells. In this chapter, I have presented the methods and some representative applications. Industrial, government and academic scientists can access STXM and ptychography at up to 20 different synchrotron facilities (see list at http://unicorn.mcmaster.ca/xrm-biblio/xrm_bib.html). More generally, for those interested in exploring SXM methods in their research, it might be useful to explore the http://lightsources.org web site, which is a clearing house for information about all 60+ synchrotron facilities worldwide, their capabilities and how to access them. Many SR facilities are upgrading to fourth generation technology, which provides a much brighter and more coherent beam, both factors which greatly enhance STXM and ptychography [9]. Over the next decade, there will be significant improvements in spatial resolution, acquisition speed and more capable instrumentation for *in situ* and *operando* studies by STXM and ptychography, all of which will significantly improve chemical analysis and imaging of PEMFC components and devices.

# Bibliography

[1]    Y. Wang, K. S. Chen, J. Mishler, S. C. Cho, and X. C. Adroher, A review of polymer electrolyte membrane fuel cells, Technology, applications, and needs on fundamental research. *Appl. Energy*, **88**, 981–1007, 2011.

[2]    M. K. Debe, Electrocatalyst approaches and challenges for automotive fuel cells. *Nature*, **486**, 43–51, 2012.

[3]    Y. Wang, D. F. Ruiz Diaz, K. S. Chen, Z. Wang, and X. C. Adroher, Materials, Technological Status, and Fundamentals of PEM Fuel Cells – A Review. *Mater. Today*, **32**, 178–203, 2020.

[4]    N. Tian, B.-A. Lu, X.-D. Yang, R. Huang, Y.-X. Jiang, Z.-Y. Zhou, and S.-G. Sun, Rational Design and Synthesis of Low-Temperature Fuel Cell Electrocatalysts. *Electrochem. Energy Rev.*, **1**, 54–83, 2018.

[5]    J. S. Walker, N. V. Rees, and P. M. Mendes, Progress towards the Ideal Core@shell Nanoparticle for Fuel Cell Electrocatalysis. *J. Exp. Nanosci.*, **13**, 258–271, 2018.

[6]    A. Z. Weber, R. L. Borup, R. M. Darling, P. K. Das, T. J. Dursch, W. Gu, D. Harvey, A. Kusoglu, S. Litster, M. M. Mench, R. Mukundan, J. P. Owejan, J. G. Pharoah, M. Secanell, and I. V. Zenyuk, Critical Review of Modeling Transport Phenomena in Polymer-Electrolyte Fuel Cells. *J. Electrochem. Soc.*, **161**, F1254, 2014.

[7]    H. Ade and A. P. Hitchcock, NEXAFS microscopy and resonant scattering: Composition and orientation probed in real and reciprocal space. *Polymer*, **49**, 643–675, 2008.

[8]    A. P. Hitchcock, Soft X-Ray Imaging and Spectromicroscopy. In: *Handbook of Nanoscopy*, pages 745–791. John Wiley & Sons, Ltd, 2012.

[9]    A. P. Hitchcock, Soft X-ray spectromicroscopy and ptychography. *J. Electron Spectrosc. Relat. Phenom.*, **200**, 49–63, 2015.

[10]   D. Susac, V. Berejnov, A. P. Hitchcock, and J. Stumper, STXM Study of the Ionomer Distribution in the PEM Fuel Cell Catalyst Layers. *ECS Trans.*, **41**, 629–635, 2011.

[11]   D. Susac, V. Berejnov, A. P. Hitchcock, and J. Stumper, STXM Characterization of PEM Fuel Cell Catalyst Layers. *ECS Trans.*, **50**, 405–413, 2013.

[12]   A. M. V. Putz, D. Susac, V. Berejnov, J. Wu, A. P. Hitchcock, and J. Stumper, Doing More with Less, Challenges for Catalyst Layer Design. *ECS Trans.*, **75**, 3–23, 2016.

[13]   D. Susac, J. Wang, Z. Martin, A. P. Hitchcock, J. Stumper, and D. Bessarabov, Chemical Fingerprint Associated with the Formation of Pt in the Membrane in PEM Fuel Cells. *ECS Trans.*, **33**, 391–398, 2010.

[14]   V. Berejnov, Z. Martin, M. West, S. Kundu, D. Bessarabov, J. Stumper, D. Susac, and A. P. Hitchcock, Probing platinum degradation in polymer electrolyte membrane fuel cells by synchrotron X-ray microscopy. *Phys. Chem. Chem. Phys.*, **14**, 4835–4843, 2012.

[15]   A. P. Hitchcock, V. Berejnov, V. Lee, M. M. West, M. Dutta, V. Colbow, and S. Wessel, Carbon corrosion of proton exchange membrane fuel cell catalyst layers studied by scanning transmission X-ray microscopy. *J. Power Sources*, **266**, 66–78, 2014.

[16]   V. Lee, D. Susac, S. Kundu, V. Berejnov, R. T. Atanasoski, A. P. Hitchcock, and J. Stumper, STXM Characterization of Nanostructured Thin Film Anode Before and After Start-Up Shutdown and Reversal Tests. *ECS Trans.*, **58**, 473–479, 2013.

[17]   V. Lee, V. Berejnov, M. West, S. Kundu, V. Berejnov, R. T. Atanasoski, A. P. Hitchcock, and J. Stumper, Scanning transmission X-ray microscopy of nano structured thin film catalysts for proton-exchange-membrane fuel cells. *J. Power Sources*, **263**, 163–174, 2014.

[18]   L. Daniel, A. Bonakdarpour, and D. P. Wilkinson, Benefits of Platinum Deposited in the Polymer Membrane Subsurface on the Operational Flexibility of Hydrogen Fuel Cells. *J. Power Sources*, **471**, 228418, 2020.

[19]   I. Martens, L. G. A. Melo, M. M. West, D. P. Wilkinson, D. Bizzotto, and A. P. Hitchcock, Imaging Reactivity of the Pt–Ionomer Interface in Fuel Cell Catalyst Layers. *ACS Appl. Energy Mater.*, **11**, 7772–7780, 2020.

[20] V. Berejnov, D. Susac, J. Stumper, and A. P. Hitchcock, 3D Chemical Mapping of PEM Fuel Cell Cathodes by Scanning Transmission Soft X-ray SpectroTomography. *ECS Trans.*, **50**, 361–368, 2013.

[21] G. Schmid, M. Obst, J. Wu, and A. P. Hitchcock, 3D Chemical Imaging of Nanoscale Biological, Environmental, and Synthetic Materials by Soft X-Ray STXM Spectrotomography. In: C. S. S. R. Kumar, Ed., *X-Ray and Neutron Techniques for Nanomaterials Characterization*, pages 43–94. Springer, Berlin, Heidelberg, 2016.

[22] J. Wu, M. Lerotic, S. Collins, R. Leary, Z. Saghi, P. Midgley, S. Berejnov, D. Susac, J. Stumper, G. Singh, and A. P. Hitchcock, Optimization of Three-Dimensional (3D) Chemical Imaging by Soft X-Ray Spectro-Tomography Using a Compressed Sensing Algorithm. *Microsc. Microanal.*, **23**, 951–966, 2017.

[23] J. Wu, L. G. A. Melo, X. Zhu, M. M. West, V. Berejnov, D. Susac, J. Stumper, and A. P. Hitchcock, 4D imaging of polymer electrolyte membrane fuel cell catalyst layers by soft X-ray spectro-tomography. *J. Power Sources*, **381**, 72–83, 2018.

[24] V. Berejnov, M. Saha, D. Susac, J. Stumper, M. West, and A. P. Hitchcock, Advances in Structural Characterization Using Soft X-ray Scanning Transmission Microscopy (STXM): Mapping and Measuring Porosity in PEMFC Catalyst Layers. *ECS Trans.*, **80**, 241–252, 2017.

[25] L. G. A. Melo, A. P. Hitchcock, J. Jankovic, J. Stumper, D. Susac, and V. Berejnov, Quantitative Mapping of Ionomer in Catalyst Layers by Electron and X-ray Spectromicroscopy. *ECS Trans.*, **80**, 275–282, 2017.

[26] L. G. A. Melo and A. P. Hitchcock, Electron Beam Damage of Perfluorosulfonic Acid Studied by Soft X-Ray Spectromicroscopy. *Micron*, **121**, 8–20, 2019.

[27] L. G. A. Melo, A. P. Hitchcock, V. Berejnov, D. Susac, J. Stumper, and G. A. Botton, Evaluating focused ion beam and ultramicrotome sample preparation for analytical microscopies of the cathode layer of a polymer electrolyte membrane fuel cell. *J. Power Sources*, **312**, 23–35, 2016.

[28] L. G. A. Melo and A. P. Hitchcock, Optimizing Soft X-ray Spectromicroscopy for Fuel Cell Studies: X-ray Damage of Ionomer. *Microsc. Microanal.*, **24**(S2), 460–461, 2018.

[29] I. Martens, L. G. A. Melo, D. P. Wilkinson, D. Bizzotto, and A. P. Hitchcock, Characterization of X-ray Damage to Perfluorosulfonic Acid Using Correlative Microscopy. *J. Phys. Chem. C*, **123**, 16023–16033, 2019.

[30] A. P. Hitchcock, Soft X-ray spectromicroscopy and ptychography. *J. Electron Spectrosc. Relat. Phenom.*, **200**, 49–63, 2015.

[31] J. Wu, X. Zhu, M. M. West, T. Tyliszczak, H.-W. Shiu, D. Shapiro, V. Berejnov, D. Susac, J. Stumper, and A. P. Hitchcock, High-Resolution Imaging of Polymer Electrolyte Membrane Fuel Cell Cathode Layers by Soft X-ray Spectro-Ptychography. *J. Phys. Chem. C*, **122**, 11709–11719, 2018.

[32] V. Berejnov, D. Susac, J. Stumper, and A. P. Hitchcock, Nano to Micro Scale Characterization of Water Uptake in The Catalyst Coated Membrane Measured by Soft X-ray Scanning Transmission X-ray Microscopy. *ECS Trans.*, **41**, 395, 2011.

[33] A. P. Hitchcock, V. Berejnov, V. Lee, D. Susac, and J. Stumper, In situ Methods for Analysis of Polymer Electrolyte Membrane Fuel Cell Materials by Soft X-ray Scanning Transmission X-ray Microscopy. *Microsc. Microanal.*, **20**, 1532–1533, 2014.

[34] J. Geilhufe, A. F. G. Leontowich, J. Wang, R. Berg, C. N. Regier, D. M. Taylor, D. Beauregard, J. Swirsky, C. Karunakaran, A. P. Hitchcock, and S. G. Urquhart, Soft X-ray Spectrotomographic Microscopy at Cryogenic Temperatures. *Microsc. Microanal.*, **24**(S2), 258–259, 2018.

[35] A. F. G. Leontowich, R. Berg, C. N. Regier, D. M. Taylor, J. Wang, D. Beauregard, J. Geilhufe, J. Swirsky, J. Wu, C. Karunakaran, A. P. Hitchcock, and S. G. Urquhart, Cryo scanning transmission x-ray microscope optimized for spectrotomography. *Rev. Sci. Instrum.*, **89**, 093704, 2018.

[36] A. P. Hitchcock, H. Yuan, L. G. A. Melo, and N. Bassim, Soft X-ray scanning transmission microscopy studies of radiation damage by electron, ion and X-ray beams. *Microsc. Microanal.*, **26**(S2), 2072–2074, 2002.

[37] B. Bozzini, A. Gianoncelli, B. Kaulich, M. Kiskinova, M. Prasciolu, and I. Sgura, Metallic Plate Corrosion and Uptake of Corrosion Products by Nafion in Polymer Electrolyte Membrane Fuel Cells. *ChemSusChem*, **3**, 846–850, 2010.

[38]   B. Bozzini, C. Mele, A. Gianoncelli, B. Kaulich, M. Kiskinova, and M. Prasciolu, In situ X-ray spectromicroscopy study of bipolar plate material stability for nano-fuel-cells with ionic-liquid electrolyte. *Microelectron. Eng.*, **88**, 2456–2458, 2011.

[39]   B. Bozzini, M. K. Abyaneh, M. Amati, A. Gianoncelli, L. Gregoratti, B. Kaulich, and M. Kiskinova, Soft X-ray Imaging and Spectromicroscopy: New Insights in Chemical State and Morphology of the Key Components in Operating Fuel-Cells. *Chemistry*, **18**, 10196–10210, 2012.

[40]   B. Bozzini, M. Amati, A. Gianoncelli, L. Gregoratti, B. Kaulich, and M. Kiskinova, New Energy Sources: in-situ Characterisation of Fuel Cell and Supercapacitor Components. Complementary Studies using Transmission, Fluorescence and Photoelectron Microscopy and Imaging. *J. Phys. Conf. Ser.*, **463**, 012018, 2013.

[41]   B. Bozzini, A. Gianoncelli, B. Kaulich, C. Mele, M. Prasciolu, and M. Kiskinova, In Situ Soft X-ray Microscopy Study of Fe Interconnect Corrosion in Ionic Liquid-Based Nano-PEMFC Half-Cells. *Fuel Cells*, **13**, 196–202, 2013.

[42]   T. Ohigashi, Y. Inagaki, T. Horigome, and N. Kosugi, Observation of Morphology of a Fuel Cell by using a humidity control sample cell for STXM. *UVSOR Annual Rep.*, **43**, 69–70, 2015.

[43]   M. G. George, J. Wang, R. Banerjee, and A. Bazylak, Composition analysis of a polymer electrolyte membrane fuel cell microporous layer using scanning transmission X-ray microscopy and near edge X-ray absorption fine structure analysis. *J. Power Sources*, **309**, 254–259, 2016.

[44]   C. J. Jacobsen, *X-ray Microscopy*. Cambridge University Press, 2019.

[45]   F. M. F. de Groot, E. de Smit, M. M. van Schooneveld, L. R. Aramburo, and B. M. Weckhuysen, In Situ Scanning Transmission X-ray Microscopy of Catalytic solds and Related Nanomaterials. *ChemPhysChem*, **11**, 951–962, 2010.

[46]   A. Braun, *X-ray Studies on Electrochemical Systems: Synchrotron Methods for Energy Materials*. Walter de Gruyter GmbH & Co KG, 2017.

[47]   M. Du and C. Jacobse, Relative Merits and Limiting Factors for X-Ray and Electron Microscopy of Thick, Hydrated Organic Materials. *Ultramicroscopy*, **184**(A), 293–309, 2018.

[48]   E. G. Rightor, A. P. Hitchcock, H. Ade, R. D. Leapman, S. G. Urquhart, A. P. Smith, G. Mitchell, D. Fischer, H. J. Shin, and T. Warwick, Spectromicroscopy of Poly(Ethylene Terephthalate): Comparison of Spectra and Radiation Damage Rates in X-Ray Absorption and Electron Energy Loss. *J. Phys. Chem. B*, **101**, 1950–1960, 1997.

[49]   J. Wang, G. A. Botton, M. M. West, and A. P. Hitchcock, Quantitative Evaluation of Radiation Damage to Polyethylene Terephthalate by Soft X-Rays and High-Energy Electrons. *J. Phys. Chem. B*, **113**, 1869–1876, 2009.

[50]   L. G. A. Melo, A. P. Hitchcock, J. Jankovic, J. Stumper, D. Susac, and V. Berejnov, Quantitative Mapping of Ionomer in Catalyst Layers by Electron and X-ray Spectromicroscopy. *ECS Trans.*, **80**, 275–282, 2017.

[51]   F. Scheiba, N. Benker, U. Kunz, C. Roth, and H. Fuess, Electron microscopy techniques for the analysis of the polymer electrolyte distribution in proton exchange membrane fuel cells. *J. Power Sources*, **177**, 273–280, 2008.

[52]   C. Wang, V. Krishnan, D. Wu, R. Bledsoe, S. J. Paddison, and G. Duscher, Evaluation of the microstructure of dry and hydrated perfluorosulfonic acid ionomers, microscopy and simulations. *J. Mater. Chem. A*, **1**, 938–944, 2012.

[53]   S. Yakovlev and K. H. Downing, Visualization of clusters in polymer electrolyte membranes by electron microscopy. *Phys. Chem. Chem. Phys.*, **15**, 1052–1064, 2012.

[54]   J. Jankovic, D. Susac, T. Soboleva, and J. Stumper, Electron Tomography Based 3D Reconstruction of Fuel Cell Catalysts. *ECS Trans.*, **50**, 353–359, 2013.

[55]   M. Holt, R. Harder, R. Winarski, and V. Rose, Nanoscale Hard X-Ray Microscopy Methods for Materials Studies. *Annu. Rev. Mater. Res.*, **43**, 183–211, 2013.

[56]   R. T. White, A. Wu, M. Najm, F. P. Orfino, M. Dutta, and E. Kjeang, 4D in situ visualization of electrode morphology changes during accelerated degradation in fuel cells by X-ray computed tomography. *J. Power Sources*, **350**, 94–102, 2017.

[57] M. Povia, J. Herranz, T. Binninger, M. Nachtegaal, A. Diaz, J. Kohlbrecher, D. F. Abbott, B.-J. Kim, and T. J. Schmidt, Combining SAXS and XAS To Study the Operando Degradation of Carbon-Supported Pt-Nanoparticle Fuel Cell Catalysts. *ACS Catal.*, **8**, 7000–7015, 2018.

[58] S. J. Normile and I. V. Zenyuk, Imaging ionomer in fuel cell catalyst layers with synchrotron nano transmission x-ray microscopy. *Solid State Ion.*, **335**, 38–46, 2019.

[59] I. V. Zenyuk, D. Y. Parkinson, G. Hwang, and A. Z. Weber, Probing water distribution in compressed fuel-cell gas-diffusion layers using X-ray computed tomography. *Electrochem. Commun.*, **53**, 24–28, 2015.

[60] T. Saida, O. Sekizawa, N. Ishiguro, M. Hoshino, K. Uesugi, T. Uruga, S. Ohkoshi, T. Yokoyama, and M. Tada, 4D Visualization of a Cathode Catalyst Layer in a Polymer Electrolyte Fuel Cell by 3D Laminography–XAFS. *Angew. Chem., Int. Ed. Engl.*, **51**, 10311–10314, 2012.

[61] H. Matsui, N. Ishiguro, T. Uruga, O. Sekizawa, K. Higashi, N. Maejima, and T. M. Operando, 3D Visualization of Migration and Degradation of a Platinum Cathode Catalyst in a Polymer Electrolyte Fuel Cell. *Angew. Chem., Int. Ed. Engl.*, **56**, 9371–9375, 2017.

[62] O. Sekizawa, T. Uruga, N. Ishiguro, H. Matsui, K. Higashi, T. Sakata, Y. Iwasawa, and M. Tada, In-situ X-ray nano-CT System for Polymer Electrolyte Fuel Cells under Operating Conditions. *J. Phys. Conf. Ser.*, **849**, 012022, 2017.

[63] W. K. Epting, J. Gelb, and S. Litster, Resolving the Three-Dimensional Microstructure of Polymer Electrolyte Fuel Cell Electrodes using Nanometer-Scale X-ray Computed Tomography. *Adv. Funct. Mater.*, **22**, 555–560, 2012.

[64] R. T. White, S. H. Eberhardt, Y. Singh, T. Haddow, M. Dutta, F. P. Orfino, and E. Kjeang, Four-Dimensional Joint Visualization of Electrode Degradation and Liquid Water Distribution inside Operating Polymer Electrolyte Fuel Cells. *Sci. Rep.*, **9**, 1843, 2019.

[65] K. Kaznacheyev, I. Blomqvist, E. Hallin, S. Urquhart, D. Loken, T. Tyliszczak, T. Warwick, and A. P. Hitchcock, Principles of Optical Design of the SM Beamline at the CLS. In: *AIP Conference Proceedings*, vol. 705, pages 1303–1307, 2004.

[66] K. V. Kaznatcheev, C. Karunakaran, U. D. Lanke, S. G. Urquhart, M. Obst, and A. P. Hitchcock, Soft X-ray spectromicroscopy beamline at the CLS: commissioning results. *Nucl. Instrum. Methods Phys. Res., Sect. A*, **582**, 96–99, 2007.

[67] D. Kilcoyne, T. Tyliszczak, W. Steele, S. Fakra, P. Hitchcock, K. Franck, E. Anderson, B. Harteneck, E. Rightor, G. Mitchell, A. P. Hitchcock, L. Yang, T. Warwick, and H. Ade, Interferometer-Controlled Scanning Transmission X-ray Microscopes at the Advanced Light Source. *J. Synchrotron Radiat.*, **10**, 125–136, 2003.

[68] K. V. Kaznacheyev, C. Karunakaran, F. He, M. Sigrist, M. Summers, M. Obst, and A. P. Hitchcock, CLS ID-10 Chicane Configuration: From "Simple Sharing" to Extended Performance with High Speed Polarization Switching, US Synchrotron Radiation Instrumentation, April 2007, Baton Rouge, LA. *Nucl. Instrum. Methods A*, **582**, 103–106, 2007.

[69] B. Rösner, S. Finizio, F. Koch, F. Döring, V. A. Guzenko, M. Langer, E. Kirk, B. Watts, M. Meyer, J. Loroña Ornelas, A. Späth, S. Stanescu, S. Swaraj, R. Belkhou, T. Ishikawa, T. F. Keller, B. Gross, M. Poggio, R. H. Fink, J. Raabe, A. Kleibert, and C. David, Soft X-Ray Microscopy with 7 nm Resolution. *Optica*, **7**, 1602–1608, 2020.

[70] C. Jacobsen, S. Wirick, G. Flynn, and C. Zimba, Soft X-ray spectroscopy from image sequences with sub-100 nm spatial resolution. *J. Microsc.*, **197**, 173–184, 2000.

[71] M. Lerotic, C. Jacobsen, T. Schäfer, and S. Vogt, Cluster analysis of soft x-ray spectromicroscopy data. *Ultramicroscopy*, **100**, 35–57, 2004.

[72] M. Lerotic, R. Mak, S. Wirick, F. Meirer, and C. Jacobsen, MANTiS: a program for the analysis of X-ray spectromicroscopy data. *J. Synchrotron Radiat.*, **21**, 1206–1212, 2014.

[73] Z. B. Yan, R. Hayes, L. G. A. Melo, G. R. Goward, and A. P. Hitchcock, X-ray Absorption and Solid-State NMR Spectroscopy of Fluorinated Proton Conducting Polymers. *J. Phys. Chem. C*, **122**, 3233–3244, 2018.

[74] A. Kusoglu and A. Z. Weber, New Insights into Perfluorinated Sulfonic-Acid Ionomers. *Chem. Rev.*, **117**, 987–1104, 2017.

[75] J. Li, A. P. Hitchcock, H. D. H. Stöver, and I. Shirley, A new approach to experimentally studying microcapsule wall growth mechanisms. *Macromolecules*, **42**, 2428–2432, 2009.

[76] K. L. More and K. S. Reeves, *Microsc. Microanal.*, **11**, 2104, 2005.

[77] D. A. Cullen, R. Koestner, R. S. Kukreja, Z. Y. Liu, S. Minko, O. Trotsenko, A. Tokarev, L. Guetaz, H. M. Meyer, C. M. Parish, and K. L. More, Imaging and Microanalysis of Thin Ionomer Layers by Scanning Transmission Electron Microscopy. *J. Electrochem. Soc.*, **161**, F1111–F1117, 2014.

[78] H. Uchida, J. M. Song, S. Suzuki, E. Nakazawa, N. Baba, and M. Watanabe, Electron Tomography of Nafion Ionomer Coated on Pt/Carbon Black in High Utilization Electrode for PEFCs. *J. Phys. Chem. B*, **110**, 13319–13321, 2006.

[79] F. I. Allen, L. R. Comolli, A. Kusoglu, M. A. Modestino, A. M. Minor, and A. Z. Weber, Morphology of hydrated as-cast Nafion revealed through cryo electron tomography. *ACS Macro Lett.*, **4**, 1–5, 2015.

[80] M. Lopez-Haro, G. L, T. Printemps, A. Morin, S. Escribano, P.-H. Jouneau, P. Bayle-Guillemaud, F. Chandezon, and G. Gebel, Three-Dimensional Analysis of Nafion Layers in Fuel Cell Electrodes. *Nat. Commun.*, **5**, 5229, 2014.

[81] S. Yakovlev, N. P. Balsara, and K. H. Downing, Insights on the Study of Nafion Nanoscale Morphology by Transmission Electron Microscopy. *Membranes*, **3**, 424–439, 2013.

[82] S. Yakovlev and K. H. Downing, Visualization of Clusters in Polymer Electrolyte Membranes by Electron Microscopy. *Phys. Chem. Chem. Phys.*, **15**, 1052–1064, 2013.

[83] L. Zielke, S. Vierrath, R. Moroni, A. Mondon, R. Zengerle, and S. Thiele, Three-Dimensional Morphology of the Interface between Micro Porous Layer and Catalyst Layer in a Polymer Electrolyte Membrane Fuel Cell. *RSC Adv.*, **6**, 80700–80705, 2016.

[84] H. Schulenburg, B. Schwanitz, N. Linse, G. G. Scherer, A. Wokaun, J. Krbanjevic, R. Grothausmann, and I. Manke, 3D Imaging of Catalyst Support Corrosion in Polymer Electrolyte Fuel Cells. *J. Phys. Chem. C*, **115**, 14236–14243, 2011.

[85] S. Zils, M. Timpel, T. Arlt, A. Wolz, I. Manke, and C. Roth, 3D Visualisation of PEMFC Electrode Structures Using FIB Nanotomography. *Fuel Cells*, **10**, 966–972, 2010.

[86] K. Karan, PEFC catalyst layer: Recent advances in materials, microstructural characterization, and modeling. *Curr. Opin. Electrochem.*, **5**, 27–35, 2017.

[87] E. H. Majlan, D. Rohendi, W. R. W. Daud, T. Husaini, and M. A. Haque, Electrode for proton exchange membrane fuel cells: A review. *Renew. Sustain. Energy Rev.*, **89**, 117–134, 2018.

[88] J. Wang, Radiation Chemistry Studied by Soft X-ray Microscopy. Ph. D. thesis, McMaster University, 2008.

[89] A. F. G. Leontowich, Tunable soft X-rays for patterning and lithography. Ph. D. thesis, McMaster University, 2012.

[90] L. G. A. Melo, Soft X-Ray Spectromicroscopy of Radiation Damaged Perfluorosulfonic Acid. Ph. D. thesis, McMaster University, 2018.

[91] J. Wang, G. A. Botton, M. M. West, and A. P. Hitchcock, Quantitative Evaluation of Radiation Damage to Polyethylene Terephthalate by Soft X-Rays and High-Energy Electrons. *J. Phys. Chem. B*, **113**, 1869–1876, 2009.

[92] J. Wang, C. Morin, L. Li, A. P. Hitchcock, X. Zhang, T. Araki, A. Doran, and A. Scholl, Radiation Damage in Soft X-ray Microscopy. *J. Electron Spectrosc. Relat. Phenom.*, **170**, 25–36, 2009.

[93] T. Coffey, S. Urquhart, and H. Ade, Characterization of the effects of soft X-ray irradiation on polymers. *J. Electron Spectrosc. Relat. Phenom.*, **122**, 65–78, 2002.

[94] V. Berejnov, B. Rubinstein, L. G. A. Melo, and A. P. Hitchcock, First principles X-ray absorption dose calculation for time dependent mass and optical density. *J. Synchrotron Radiat.*, **25**, 833–847, 2018.

[95] V. Berejnov, B. Rubinstein, L. G. A. Melo, and A. P. Hitchcock, Calculating Absorption Dose When X-ray Irradiation Modifies Material Quantity and Chemistry. *J. Synchrotron Radiat.*, **28**, 834–838, 2021.

[96] T. Xie and C. A. Hayden, A kinetic model for the chemical degradation of perfluorinated sulfonic acid ionomers: Weak end groups versus side chain cleavage. *Polymer*, **48**, 5497–5506, 2007.

[97] L. Ghassemzadeh, K. D. Kreuer, J. Maier, and K. Müller, Evaluating Chemical Degradation of Proton Conducting Perfluorosulfonic Acid Ionomer in a Fenton Test by Solid-state $^{19}$F NMR Spectroscopy. *J. Power Sources*, **196**, 2490–2497, 2011.

[98] K. Hongsirikarn, X. Mo, J. Goodwin, and S. Creager, Effect of $H_2O_2$ on Nafion (R) Properties and Conductivity at Fuel Cell Conditions. *J. Power Sources*, **196**, 3060–3072, 2011.

[99] G. A. Johansson, T. Tyliszczak, G. E. Mitchell, M. H. Keefe, and A. P. Hitchcock, Three-dimensional chemical mapping by scanning transmission X-ray spectromicroscopy. *J. Synchrotron Radiat.*, **14**, 395–402, 2007.

[100] E. Y. Sidky and X. Pan, Image Reconstruction in Circular Cone-Beam Computed Tomography by Constrained, Total-Variation Minimization. *Phys. Med. Biol.*, **53**, 4777–4807, 2008.

[101] K. Witte, A. Späth, S. Finizio, C. Donnelly, B. Watts, B. Sarafimov, M. Odstrcil, M. Guizar-Sicairos, M. Holler, R. H. Fink, and J. Raabe, From 2D STXM to 3D Imaging: Soft X-ray Laminography of Thin Specimens. *Nano Lett.*, **20**, 1305–1314, 2020.

[102] F. Pfeiffer and X. Ptychography, *Nat. Commun.*, **12**, 9–17, 2018.

[103] O. Mandula, M. Elzo Aizarna, J. Eymery, M. Burghammer, and V. Favre-Nicolin, PyNX.Ptycho: A Computing Library for X-Ray Coherent Diffraction Imaging of Nanostructures. *J. Appl. Crystallogr.*, **49**, 1842–1848, 2016.

[104] S. Marchesini, H. Krishnan, B. J. Daurer, D. A. Shapiro, T. Perciano, J. A. Sethian, and F. R. N. C. Maia, SHARP: a distributed, GPU-based ptychographic solver. *J. Appl. Crystallogr.*, **49**, 1245–1252, 2016.

[105] B. Enders and P. Thibault, A Computational Framework for Ptychographic Reconstructions. *Proc. R. Soc. A*, **472**, 20160640, 2016.

[106] M. Farmand, R. Celestre, P. Denes, A. L. D. Kilcoyne, S. Marchesini, H. Padmore, T. Tyliszczak, T. Warwick, X. Shi, J. Lee, Y.-S. Yu, J. Cabana, J. Joseph, H. Krishnan, T. Perciano, F. R. N. C. Maia, and D. A. Shapiro, Near-Edge X-Ray Refraction Fine Structure Microscopy. *Appl. Phys. Lett.*, **110**, 063101, 2017.

[107] D. A. Shapiro, Y.-S. Yu, T. Tyliszczak, J. Cabana, R. Celestre, W. Chao, K. Kaznatcheev, A. L. D. Kilcoyne, F. Maia, S. Marchesini, Y. S. Meng, T. Warwick, L. L. Yang, and H. A. Padmore, Chemical composition mapping with nanometre resolution by soft X-ray microscopy. *Nat. Photonics*, **8**, 765–769, 2014.

[108] D. A. Shapiro, S. Babin, R. S. Celestre, W. Chao, R. P. Conley, P. Denes, B. Enders, P. Enfedaque, S. James, J. M. Joseph, H. Krishnan, S. Marchesini, K. Muriki, K. Nowrouzi, S. R. Oh, H. A. Padmore, T. Warwick, L. Yang, V. V. Yashchuk, Y.-S. Yu, and J. Zhao, An Ultrahigh-Resolution Soft x-Ray Microscope for Quantitative Analysis of Chemically Heterogeneous Nanomaterials. *Sci. Adv.*, **6**, eabc490, 2020.

[109] H. Yuan, H. Yuan, T. Casagrande, D. A. Shapiro, Y.-S. Yu, B. Enders, J. R. I. Lee, T. Van Buuren, M. M. Biener, S. A. Gammon, T. T. Li, T. F. Baumann, and A. P. Hitchcock, 4D Imaging of ZnO-Coated Nanoporous $Al_2O_3$ Aerogels by Chemically-Sensitive Ptychographic Tomography: Implications for Designer Catalysts. *ACS Appl. Nanomater.*, **4**, 621–632, 2021.

[110] T. Beetz and C. Jacobsen, Soft X-ray radiation-damage studies in PMMA using a cryo-STXM. *J. Synchrotron Radiat.*, **10**, 280–283, 2002.

[111] K.-H. Kim, K.-Y. Lee, H.-J. Kim, E. Cho, S.-Y. Lee, T.-H. Lim, S. P. Yoon, I. C. Hwang, and J. H. Jang, The Effects of Nafion® Ionomer Content in PEMFC MEAs Prepared by a Catalyst-Coated Membrane (CCM) Spraying Method. *Int. J. Hydrog. Energy*, **35**, 2119–2126, 2010.

[112] S. Mu and M. Tian, Optimization of Perfluorosulfonic Acid Ionomer Loadings in Catalyst Layers of Proton Exchange Membrane Fuel Cells. *Electrochim. Acta*, **60**, 437–442, 2012.

[113] A. P. Hitchcock, V. Lee, J. Wu, M. M. West, G. Cooper, V. Berejnov, T. Soboleva, D. Susac, and J. Stumper, Characterizing automotive fuel cell materials by soft x-ray scanning transmission x-ray microscopy. *AIP Conf. Proc.*, **1696**, 020012, 2016.

[114] Z. Chen and H. R. Catalyst, Support Degradation. In: *PEM Fuel Cell Failure Mode Analysis*. CRC Press, FL, USA, 2011.

[115]   C. Qin, J. Wang, D. Yang, B. Li, and C. Zhang, Proton Exchange Membrane Fuel Cell Reversal: A Review. *Catalysts*, **6**, 197, 2016.

[116]   F. Ettingshausen, J. Kleemann, A. Marcu, G. Toth, H. Fuess, and C. Roth, Dissolution and Migration of Platinum in PEMFCs Investigated for Start/Stop Cycling and High Potential Degradation. *Fuel Cells*, **11**, 238–245, 2011.

[117]   M. Prokop, T. Bystron, P. Belsky, O. Tucek, R. Kodym, M. Paidar, and K. Bouzek, Degradation Kinetics of Pt during High-Temperature PEM Fuel Cell Operation Part III: Voltage-Dependent Pt Degradation Rate in Single-Cell Experiments. *Electrochim. Acta*, **363**, 137165, 2020.

[118]   N. Macauley, D. D. Papadias, J. Fairweather, D. Spernjak, D. Langlois, R. Ahluwalia, K. L. More, R. Mukundan, and R. L. Borup, Carbon Corrosion in PEM Fuel Cells and the Development of Accelerated Stress Tests. *J. Electrochem. Soc.*, **165**, F3148–F3160, 2018.

[119]   L. Helfen, A. Myagotin, P. Mikulík, P. Pernot, A. Voropaev, M. Elyyan, M. Di Michiel, J. Baruchel, and T. Baumbach, On the Implementation of Computed Laminography Using Synchrotron Radiation. *Rev. Sci. Instrum.*, **82**, 063702, 2011.

[120]   S. Deabate, G. Gebel, P. Huguet, A. Morin, and G. Pourcelly, In Situ and Operando Determination of the Water Content Distribution in Proton Conducting Membranes for Fuel Cells: A Critical Review. *Energy Environ. Sci.*, **5**, 8824–8847, 2012.

[121]   Q. Meyer, Y. Zeng, and C. Zhao, In Situ and Operando Characterization of Proton Exchange Membrane Fuel Cells. *Adv. Mater.*, **31**, 1901900, 2019.

[122]   L. Wang, J. Wang, and P. Zuo, Probing Battery Electrochemistry with In Operando Synchrotron X-Ray Imaging Techniques. *Small Methods*, **2**, 1700293, 2018.

[123]   D. Liu, Z. Shadike, R. Lin, K. Qian, H. Li, K. Li, S. Wang, Q. Yu, M. Liu, S. Ganapathy, X. Qin, Q.-H. Yang, M. Wagemaker, F. Kang, X.-Q. Yang, and B. Li, Review of Recent Development of In Situ/Operando Characterization Techniques for Lithium Battery Research. *Adv. Mater.*, **31**, 1806620, 2019.

[124]   J. Li and J. Gong, Operando Characterization Techniques for Electrocatalysis. *Energy Environ. Sci.*, **13**, 3748–3779, 2020.

[125]   M. Ji and Z. Wei, A Review of Water Management in Polymer Electrolyte Membrane Fuel Cells. *Energies*, **2**, 1057–1106, 2009.

[126]   M. Sahraoui, Y. Bichiou, and K. Halouani, Three-Dimensional Modeling of Water Transport in PEMFC. *Int. J. Hydrog. Energy*, **38**, 8524–8531, 2012.

[127]   Y.-S. Yu, C. Kim, D. A. Shapiro, M. Farmand, D. Qian, T. Tyliszczak, A. L. D. Kilcoyne, R. Celestre, S. Marchesini, J. Joseph, P. Denes, T. Warwick, F. C. Strobridge, C. P. Grey, H. A. Padmore, Y. S. Meng, R. Kostecki, and J. Cabana, Dependence on Crystal Size of the Nanoscale Chemical Phase Distribution and Fracture in $Li_xFePO_4$. *Nano Lett.*, **15**, 4282–4288, 2015.

[128]   Y. Li, J. N. Weker, W. E. Gent, D. N. Mueller, J. Lim, D. A. Cogswell, T. Tyliszczak, and W. C. Chueh, Dichotomy in the Lithiation Pathway of Ellipsoidal and Platelet LiFePO4 Particles Revealed through Nanoscale Operando State-of-Charge Imaging. *Adv. Funct. Mater.*, **25**, 3677–3687, 2015.

[129]   M. Wolf, B. M. May, and J. Cabana, Visualization of Electrochemical Reactions in Battery Materials with X-Ray Microscopy and Mapping. *Chem. Mater.*, **29**, 3347–3362, 2017.

[130]   B. Bozzini, M. Kazemian, M. Kiskinova, G. Kourousias, C. Mele, and A. Gianoncelli, Operando Soft X-Ray Microscope Study of Rechargeable Zn–Air Battery Anodes in Deep Eutectic Solvent Electrolyte. *X-Ray Spectrom.*, **48**, 527–535, 2019.

[131]   A. F. G. Leontowich and A. P. Hitchcock, Experimental investigation of beam heating in a soft X-ray scanning transmission X-ray microscope. *Analyst*, **137**, 370–375, 2012.

[132]   T. Lefevre, M. Pézolet, D. Hernández Cruz, M. M. West, M. Obst, A. P. Hitchcock, C. Karunakaran, and K. V. Kaznatcheev, Mapping molecular orientation in dry and wet dragline spider silk. *J. Phys. Conf. Ser.*, *Proc. 9th Int. Conf. on X-ray Microscopy*, **186**, 012089, 2009.

[133]   S. T. Kelly, P. Nigge, S. Prakash, A. Laskin, B. Wang, T. Tyliszczak, S. R. Leone, and M. K. Gilles, An environmental sample chamber for reliable scanning transmission x-ray microscopy measurements under water vapor. *Rev. Sci. Instrum.*, **84**, 073708, 2013.

[134] C. Gosse, S. Stanescu, J. Frederick, S. Lefrançois, A. Vecchiola, M. Moskura, S. Swaraj, R. Belkhou, B. Watts, P. Haltebourg, C. Blot, J. Daillant, P. Guenoun, and C. A. Chevallard, Pressure-Actuated Flow Cell for Soft X-Ray Spectromicroscopy in Liquid Media. *Lab Chip*, **20**, 3213–3229, 2020.

[135] D. Guay, J. Stewart-Ornstein, X. Zhang, and A. P. Hitchcock, In situ spatial and time resolved studies of electrochemical reactions by scanning transmission X-ray microscopy. *Anal. Chem.*, **77**, 3479–3487, 2005.

[136] B. Bozzini, L. D'Urzo, A. Gianoncelli, B. Kaulich, M. Kiskinova, M. Prasciolu, and A. Tadjeddine, In Situ Soft X-Ray Dynamic Microscopy of Electrochemical Processes. *Electrochem. Commun.*, **10**, 1680–1683, 2008.

[137] Y. A. Wu, Z. Yin, M. Farmand, Y.-S. Yu, D. A. Shapiro, H.-G. Liao, W.-I. Liang, Y.-H. Chu, and H. Zheng, In-Situ Multimodal Imaging and Spectroscopy of Mg Electrodeposition at Electrode-Electrolyte Interfaces. *Sci. Rep.*, **7**, 42527, 2017.

[138] V. Prabu, M. Obst, H. Hosseinkhannazer, M. Reynolds, S. Rosendahl, J. Wang, and A. P. Hitchcock, Instrumentation for in situ flow electrochemical Scanning Transmission X-ray Microscopy (STXM). *Rev. Sci. Instrum.*, **89**, 063702, 2018.

[139] J. Parrondo, M. Ortueta, and F. Swelling, Swelling Behavior of PEMFC during Conditioning. *Braz. J. Chem. Eng.*, **24**, 411–419, 2007.

[140] N. Hodnik, G. Dehm, and K. J. J. Mayrhofer, Importance and Challenges of Electrochemical in Situ Liquid Cell Electron Microscopy for Energy Conversion Research. *Acc. Chem. Res.*, **49**, 2015–2022, 2016.

[141] A. Siebel, Y. Gorlin, J. Durst, O. Proux, F. Hasché, M. Tromp, and H. A. Gasteiger, Identification of Catalyst Structure during the Hydrogen Oxidation Reaction in an Operating PEM Fuel Cell. *ACS Catal.*, **6**, 7326–7334, 2016.

[142] Y. Wu and N. Liu, Visualizing Battery Reactions and Processes by Using In Situ and In Operando Microscopies. *Chem*, **4**, 438–465, 2018.

[143] R. Banerjee, N. Ge, C. Han, J. Lee, M. G. George, H. Liu, D. Muirhead, P. Shrestha, and A. Bazylak, Identifying in Operando Changes in Membrane Hydration in Polymer Electrolyte Membrane Fuel Cells Using Synchrotron X-Ray Radiography. *Int. J. Hydrog. Energy*, **43**, 9757–9769, 2018.

[144] J. Eller, F. Marone, and F. N. Büchi, Operando sub-second tomographic imaging of water in pefc gas diffusion layers. *ECS Trans.*, **69**, 523–531, 2015.

[145] A. Schneider, C. Wieser, J. Roth, and L. Helfen, Impact of synchrotron radiation on fuel cell operation in imaging experiments. *J. Power Sources*, **195**, 6349–6355, 2010.